JM PAPERS

Accelerating turbulence in heated micron tubes at supercritical pressure

Yuli Cao[1]**, Ruina Xu**[1]**, S. He**[2] **and Peixue Jiang**[1]**,†**

[1]Department of Energy and Power Engineering, Tsinghua University, PR China
[2]Departmen of Mechanical Engineering, University of Sheffield, Sheffield S1 3JD, UK

The purpose of this research was to provide further understanding of turbulent dynamics and heat transfer mechanisms in accelerating flows with thermophysical variations and pressure drops in micron tubes. Direct numerical simulations were conducted to investigate the turbulence to supercritical pressure CO_2 in heated micron tubes with inner diameter 99.2 μm. In general, the turbulent heat transfer enhancement/deterioration at supercritical pressure is dominated by variations in thermophysical properties, buoyancy and thermal acceleration; however, the mechanism differs in micron tubes ($d^* < 100$ μm). The results showed that the pressure drop and scale effect made significant contributions to the development of turbulence flows heated at supercritical pressure in micron tubes, leading to the prominent property change and flow acceleration in the inlet fully developed turbulent flow. The deviation on temperature distribution because of pressure changes was non-negligible. The primary contribution of the acceleration was the decay of a boundary layer, which significantly suppressed the production of turbulence and decreased heat transfer. The acceleration had stabilizing effects on the ejection and sweep motions of the turbulent flow. The high-speed fluid contributed to a new disturbance scenario of the flow with a larger spanwise wavenumber superimposed on existing perturbations. The high-speed streak width in the quasilaminar region was approximately 150–$160\nu/u_\tau$ in accelerating flow. In the micron tubes, the Reynolds stress events of quadrant Q4 contributed 60 % of the Reynolds stress, greater than those of quadrant Q2.

Key words: stratified turbulence, vortex breakdown, turbulence simulation

1. Introduction

Supercritical pressure fluids are used as working fluids in many industrial applications, such as advanced nuclear reactors, transcritical CO_2 refrigeration system, platelet transpiration cooling methods and solar-thermal power stations (Mao *et al.* 2021; Ehsan

† Email address for correspondence: jiangpx@tsinghua.edu.cn

et al. 2023). Advanced platelet transpiration cooling methods are intended to protect surfaces with significant thermal loads, such as walls in rocket thrust chambers at high operating temperatures (May & Burkhardt 1991; Yin & Liu 2018). Platelet cooling technology has been developed as a very flexible thermal management method by designing diffusion bonding together thin metal platelets which contain etched coolant passages. The coolant passages are generally very small, from a dozens of microns to hundreds of microns range (Mueggenburg *et al.* 2010). The advanced supercritical CO_2 Braydon cycle has gained much interest in renewable energy systems to improve the cycle efficiency. The design method of the high-efficiency compact heat exchanger of high efficiency and compactness is the focal point (Robey *et al.* 2022). In view of increasing power density and higher integration degree of electric technology, microchannel heat sink is a promising technology for power electronics cooling. Compared with traditional refrigerants, supercritical CO_2 is promising as a heat transfer fluid in microchannel heat sink (Leng *et al.* 2016). In the above advanced technologies, the supercritical pressure fluids often flow through micron-scale channels with high heat fluxes at the surfaces and present very advantageous but complicated flow and heat transfer characteristics.

A variety of technologies have been developed to combat new challenges of extreme thermal loads, including thermoelectric, two-phase and supercritical technologies. Turbulent convection cooling in microchannels is one of the practical threads of technology (Zeighami *et al.* 2000), since the commonly used single-phase laminar convection are not in the position to address the heat removal needs. From the 1990s, many microchannel cooling studies have utilized turbulent convection in micron-scale channels; both theoretical models and experimental investigations have been reported (Phillips 1990; Hegab, Ban & Ameel 2002). As a result, the turbulent heat transfer and pressure drop characteristics of the supercritical pressure fluids in micron-scale channels are of significance to the development of future energy and power systems using supercritical pressure fluids.

The major reason that the heat transfer characteristics can be very complicated is the drastic thermophysical properties variation within small temperature and pressure changes as shown in figure 1. Variations in the thermophysical properties of supercritical pressure fluids directly influence the heat transfer ability. For example, the increase in specific heat and thermal conductivity will enhance the heat transfer near the pseudocritical point. When a pure substance is heated in a constant-pressure process at a pressure greater than the critical point, there are no two phases present. But there is a continuous change in molecular organization structure, resulting in continuous changes in physical property (Yoo 2013). The pseudocritical point (T_{pc}, P_{pc}) corresponds to the maximum value of specific heat at this particular pressure. In addition, changes in temperature or pressure cause non-uniform distributions of thermophysical properties that not only directly influence other properties, but also contribute to buoyancy and flow acceleration and thereby induce abnormal turbulent dynamics and heat transfer phenomena.

Convective heat transfer to supercritical pressure fluids has been investigated since the 1950s by many researchers for applications of supercritical fluids in various industrial fields (Krasnoshchekov & Protopopov 1966; Hall 1971; Petukhov 1977; Petukhov, Polyakov & Launder 1988; Jackson 2001; Jiang *et al.* 2004). The working fluids have mostly been water, carbon dioxide and hydrocarbon fuels. Over time, extensive experimental studies have been developed, and they have provided comprehensive quantitative and qualitative insights into the complicated heat transfer characteristics of supercritical pressure fluids (Kirillov, Yur'ev & Bobkov 1990; Jackson 2002; Liao & Zhao 2002; Kim, Jeon & Lee 2007; Kim *et al.* 2008). The previous studies showed that the
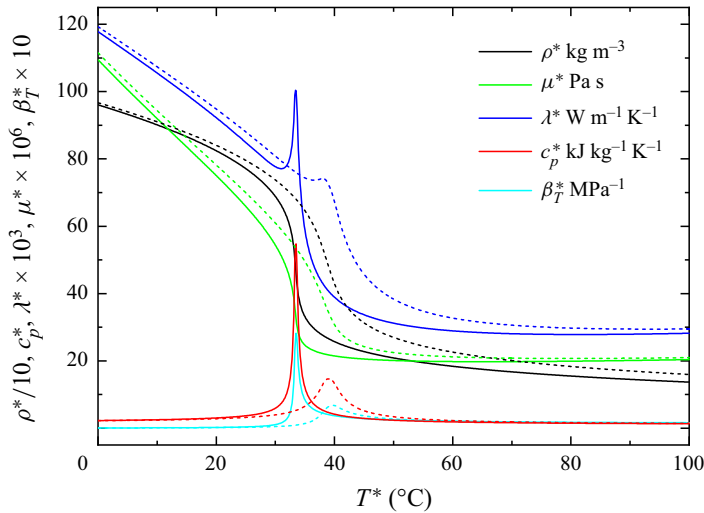
Figure 1. Thermophysical properties of supercritical pressure CO_2 at 7.8 MPa (solid lines) and 8.8 MPa (dashed lines).

turbulent heat transfer characteristics of supercritical pressure fluid could be especially complex and difficult to predict. The complicated heat transfer behaviour, including deterioration, recovery and enhancement mainly resulted from the violent thermophysical property variations, buoyancy and acceleration of the bulk flow. To understand the mechanism of the turbulent heat transfer of supercritical pressure flow, it is important to figure out how the turbulence dynamics are affected.

The turbulent heat transfer rules under different pipe diameters are significantly different. Several theories have been proposed for the mechanism for turbulent convective heat transfer of fluid at supercritical pressure in different conditions. With the decrease of pipe diameter, the effect of buoyancy decreases and the effect of flow acceleration increases. The characteristics of supercritical pressure flow at low Reynolds number in tubes with diameter of tens of millimetres were found to be influenced by buoyancy and thermophysical properties. In millimetre-scale tubes, the turbulent convection is influenced by coupling effects of buoyancy and thermal acceleration. In the micron-scale tubes, flow acceleration and scale effect will induce more complicated flow and heat transfer characteristics, which is not yet fully understood. Numerical simulation has been regarded as a method to help understand the phenomenon and mechanisms of supercritical heat transfer (Bae, Yoo & Mceligot 2008; He, Kim & Bae 2008; Mohseni & Bazargan 2011; Nemati *et al.* 2015; Peeters *et al.* 2016; Jiang, Wang & Xu 2018; Cao *et al.* 2021; He *et al.* 2021). Herein, we would like to give a brief introduction to current knowledge of turbulent dynamics of heated flows at supercritical pressures and to set the scene for the research in this present paper.

Several numerical studies have investigated the effects of variations in thermophysical properties on turbulent dynamics (Zonta, Marchioli & Soldati 2012*a*; Lee *et al.* 2013; Zonta 2013; Zonta & Soldati 2014; Patel *et al.* 2015). Zonta *et al.* (2012*a*) reported that the characteristics of streaks are affected by variations in viscosity. The authors showed that high- and low-viscosity regions dampen and enhance the intensity of turbulence, which has a large influence on momentum and heat transfer in channel flows. Patel *et al.* (2015) found that the stability of streaks was significantly affected by mean density and

viscosity stratification. These studies have indicated that strong variations in properties had a profound effect on turbulent dynamics, whereas it was not very clear whether these were direct effects of changes in thermophysical properties or indirect effects of induced buoyancy and flow acceleration.

Besides the Reynolds-averaged Navier–Stokes simulations, many direct numerical simulation (DNS) studies have contributed to the establishment of the general understanding of a mechanism of property variations. Nemati *et al.* (2015) studied the effects of buoyancy and large thermophysical property variations on mean flow statistics and reported that property fluctuations had a small effect on mean momentum and a large effect on energy budgets of Reynolds stresses. Peeters *et al.* (2016) conducted a DNS of supercritical fluid flow in an annular channel with a hot outer wall and a cool inner wall to study the buoyancy effect in aiding and opposing flows. Turbulence was significantly decreased near the hot wall but increased near the cold wall; this was only partially attributed to the effects of mean dynamic viscosity and density variations. The authors concluded that near the pseudocritical temperature, the structural effect decreased because the temperature fluctuation diminished, but in contrast, it became effective when the heat capacity was smaller. Furthermore, Azih & Yaras (2018) investigated the structural effect of density variations on the topology of turbulence in heated channel flow of supercritical fluids. It was shown that the reduction in density and viscosity in forced convection contributed to the generation of small-scale vortices and the interaction and breakage of existing large near-wall structures, which resulted in a reduction in turbulent mixing. He *et al.* (2021) proposed a new understanding of turbulent dynamics in a heated flow of fluid at supercritical pressure by treating the various factors (i.e. variable viscosity, buoyancy and thermal expansion) as pseudo-body forces. The effect of pseudo-body forces caused a reduction in the so-called apparent Reynolds number, which led to the turbulence attenuation. In their study, the partially laminarizing flow was represented by a reference flow with equivalent pressure gradient plus a flow perturbation. Their conclusion about the effect of buoyancy on turbulent dynamics was consistent with the results of previous studies under similar conditions. However, the present studies mainly considered the fluid properties variations with temperature changes under constant wall temperature or constant heat flux boundary condition. There is a gap in the research of the mechanisms of pressure changes which caused physical property variations on the turbulent heat transfer.

The buoyancy effect caused by density gradient on turbulent mixed convective in millimetre-scale tubes has received considerably more attention. The buoyancy effect makes an interesting contribution in terms of decreasing convective heat transfer due to turbulence, recovery and enhancement by influencing the intensity and structures of turbulence. An early explanation of the mechanism involved was given by Hall & Jackson (1969). They suggested that the dominant factor was the modification of the shear stress distribution across the pipe, with a consequent change in turbulence production. In a follow-up study (Petukhov *et al.* 1988), the authors further analysed the effect of buoyancy on the dynamics of turbulence and proposed that the influence of buoyancy forces can be characterised into two ways as a structural (direct) effect and an external (indirect) effect. The former refers to the effect of the interactions between the fluctuating buoyancy force and velocity $\overline{\rho'u'}$, which is quantified by the buoyancy production term in the turbulent kinetic energy equation. The external effect refers to the fact that buoyancy acting as a body force distorts the mean velocity profile by local flow acceleration or deceleration, which in turn results in a change in turbulence shear stress production. Bae, Yoo & Choi (2005) further noted that turbulent heat transfer is recovered and even enhanced as the

turbulence regeneration restored, when the mean velocity distribution is deformed into an M-shaped profile in upward flow.

However, there are far fewer investigations into the effect of flow acceleration than the effect of the buoyancy effect on convective heat transfer by turbulent flow. Flow acceleration including thermal expansion is usually not a strong effect compared with the buoyancy effect in tubes and channels with large diameters (e.g. $d_{in} > 1$ mm), as concluded by Jiang *et al.* (2010). Their experimental results indicated that for all flow orientations, the local Nusselt number decreased substantially with decreasing diameter submillimetre tubes (e.g. $d_{in} = 0.27$ mm), which differed from results for normal size tubes due to flow acceleration. In the study of Peeters *et al.* (2016), the annular flows with hot and cool walls enable the authors to study the influence of both thermal expansion and buoyancy on the evolution of streamwise coherent structures. The authors demonstrated that near the hot wall, both thermal expansion and buoyancy had negative impacts on coherent streak flank strength. They noted that the thermal expansion had the largest influence. For millimetre-scale channels, Cao *et al.* (2021) conducted a DNS study of convective heat transfer of supercritical pressure CO_2 in a heated vertical tube with $d^* = 1$ mm, with coupling buoyancy and thermal acceleration effects. The authors observed that under the coupled effects, the turbulent flow and heat transfer exhibited four periods of development in which buoyancy and thermal acceleration alternately dominated. The results indicated that the local flow acceleration induced a stretch-to-disrupt mechanism of coherent turbulent structures. The previous study illustrated the coupling mechanism of buoyancy and thermal acceleration. For submillimetre and micron-scale channels, the coupling effects turn to flow acceleration and scale effect where pressure drops could not be ignored. Compared with studies of the effect of buoyancy on heat transfer, there are relatively few studies on the deterioration of local heat transfer caused by flow acceleration in submillimetre and micron-scale channels.

Previous studies in normal-size channels generally ignored the pressure drop along the flow direction. However, the pressure drops would substantially increase in smaller channels. Though the hydraulic resistance is conventionally increased in turbulence regime and higher pumping powers are required, the turbulence convection in micron channels is necessary for future cooling technologies. Within last three decades, much research has been done on turbulent flow in microchannels with diameter of several microns to hundreds of microns using subcritical pressure refrigerant. The research studied the details relevant for microchannel convection and focused on the transition from laminar flow to turbulence. Peng, Peterson & Wang (1994) studied the pressure drop along channels with hydraulic diameters from 133 to 367 µm and found the transition Reynolds number, $200 < Re_{tr} < 700$. Yu *et al.* (1995) studied the fluid flow and heat transfer characteristics of dry nitrogen gas and water in pipe of diameters from 19 to 102 µm. The results indicated that turbulent Nusselt numbers in the microchannel were higher than that for larger tubes, suggesting that the Reynolds analogy does not hold for microchannel flow. Zeighami *et al.* (2000) studied turbulent transition in a 120 µm microchannel at various Reynolds numbers using micron-resolution particle imaging velocimetry. The velocity field data suggest transition for $1200 < Re_{tr} < 1600$, their study provided a direct flow field measurements for a more rigorous study of flow transition in microchannels. In recent years, more experimental investigations about the turbulent mechanism for heat and momentum transfer in microchannels showed that both channel size and surface roughness have remarkable effects on the performance of flow behaviour and heat transfer (Lee, Garimella & Liu 2005; Ahmad, Hassan & Megahed 2015; Jajja, Zada & Fronk 2019).

The prediction of turbulent heat transfer in microchannels differs in microchannels from macrochannels.

As for turbulence flows at supercritical pressure, the high specific heat capacity and low viscosity characteristics are beneficial to reduce the pressure drop. But the mechanism of pressure drop influence on the turbulence convection is not clear. Most numerical research on turbulent heat transfer of supercritical pressure fluids was conducted in normal-size channels with the assumption of thermodynamically constant pressure, which determines all thermodynamic state variables at a constant thermodynamic pressure, P_0. Recognizing the apparent lack of systematic research on heat and momentum transport in microchannels, Jiang *et al.* (2010, 2013) and Liao & Zhao (2002) conducted experimental investigations of heat transfer and pressure drops characteristics in micron-scale pipes. They concluded that the thermodynamic pressure change was non-negligible when the tube is micron-scale or the ratio of heat flux to mass flow rate was large and a thermophysical pressure change occurred in the tube. According to Jiang *et al.* (2010, 2013), the thermophysical pressure change consists of pressure drops due to friction and acceleration, which can be of the same order of magnitude as the inlet pressure and have a significant effect on the heat transfer of supercritical fluids. The pressure drop contributes to significant global flow acceleration as well as thermal acceleration caused by the temperature gradient in the heated tube flow since density changes with pressure and temperature. In summary, the decrease in heat transfer caused by global flow acceleration is different from that caused by the buoyancy effect. Lack of understanding of this behaviour is responsible for lack of a corresponding predictive method. Thus, there is a need for more studies and better understanding of heat transfer in submillimetre and micron-scale channels.

In this paper, we aim to investigate the mechanisms of turbulence attenuation and heat transfer deterioration in a micron-scale tube at supercritical pressure. Based on our previous study in millimetre-scale tubes (Cao *et al.* 2021), the DNS method has been modified to conduct simulations of supercritical pressure fluid flow in a heated micron tube with an inner diameter of $99.2\,\mu\text{m}$ while considering the pressure variation along the heated section. The thermophysical property variations with pressure as well as temperature are included, and the pressure gradient term in the energy equation is considered. First, we investigated how thermophysical property variation, both the mean variation and its fluctuation, affects the turbulent heat transfer characteristics. Comparisons of numerical predictions with experimental data are provided. Second, an understanding was developed of how flow acceleration affects turbulent motion in a qualitative as well as a quantitative manner, including thermal expansion and pressure drop acceleration. Finally, the generation of turbulence structures under scale effect in micron-scale tube was investigated.

2. Methodology

2.1. *Governing equations*

The simulations were performed using the code CHAPSim, which is first developed by Seddighi (2011). In this study, the code was modified to consider the pressure change in the micron-scale tube, as well as thermophysical property variation due to the pressure change of supercritical pressure fluid flow. Near the critical point, the amplitude of the density fluctuations increases with the associated correlation length ξ, and L is the length scale of the given volume. According to the experimental results of Nishikawa, Tanaka & Amemiya (1996), the assumption of local thermodynamic equilibrium is valid in this

paper with the scale

$$L \gg \xi \tag{2.1}$$

Therefore, we assumed that the heated CO_2 flow at supercritical pressure under investigation may be considered to be in local thermodynamic equilibrium, which indicated that the hydrodynamic equations apply fully (Zappoli, Beysens & Garrabos 2014). Under this assumption, the fluid state was described by the hydrodynamic conservation equations written for a viscous, highly expandable fluid with low heat diffusivity, also referred to as a low-Mach number flow.

In the following discussion, the superscript $*$ denotes the dimensional quantities and the subscript 0 denotes the values at the pipe inlet. To derive the low-Mach number equations, one expands the pressure P^* as a power series in $\varepsilon = \lambda M^2$, the ratio of the dynamic to the thermodynamic pressure. In the definition, $\gamma = c_p^*/c_v^*$ is the ratio of specific heats, and $M = U_b^*/a^*$ is the Mach number, a^* is the sound velocity:

$$
\begin{aligned}
P^* &= \frac{1}{\varepsilon}\rho^{*(0)}T^{*(0)} + \rho^{*(1)}T^{*(0)} + \rho^{*(0)}T^{*(1)} + \cdots \\
&= \frac{1}{\varepsilon}P^{*(0)} + P^{*(1)} + \cdots .
\end{aligned}
\tag{2.2}
$$

Equation (2.2) states that the pressure is decomposed of a thermodynamic part $P^{*(0)}$ and a hydrodynamic part $P^{*(1)}$. Obviously, ε is a small parameter in a low Mach number flow, and the hydrodynamic pressure is assumed to be very small compared with the thermodynamic pressure. Thus, all thermophysical property variations due to hydrodynamic pressure fluctuations can be neglected. This would mean that thermodynamic variables such as density, temperature, enthalpy and entropy could be determined as functions of thermophysical pressure and enthalpy; for example,

$$\rho^*(P^*, h^*) = \rho^*(P^{*(0)}, h^*). \tag{2.3}$$

In addition, the viscous heating term in the energy equation is off, and it is eliminated in the limit of low Mach numbers. We aimed to investigate heated CO_2 flows at 7.8 and 8.8 MPa, for which the speed of sound has the minimum value of $173 \, \mathrm{m \, s^{-1}}$. Considering bulk velocities of $3 \, \mathrm{m \, s^{-1}}$, the Mach number is less than 0.02, which validates the uses of the low-Mach number assumption. By neglecting the hydrodynamic pressure change, the total pressure change used to evaluate a thermophysical property for supercritical pipe flow is decomposed into three terms from the following equation:

$$\Delta P_{total}^* = \Delta P_f^* + \Delta P_g^* + \Delta P_a^*. \tag{2.4}$$

The first term on the right-hand side is the friction pressure drop along the pipe, ΔP_f^*. According to the friction law for smooth pipes, the friction factor $f \equiv (\Delta P_f^* D^*)/(1/2\rho^*\bar{U}^{*2}L^*)$ of the smooth pipe flow is implicitly a function of $Re = \rho^*\bar{U}^{*2}L^*/\mu^*$, where D^* is the diameter of the pipe. This indicates that at a specified inlet Re_0, the fractional pressure drop ΔP_f^* over an axial distance L for pipe flow is proportional to D^{*-3}. The acceleration pressure drop ΔP_a^* between the inlet and exit, it can be calculated by invoking an energy balance along the heated test section $\Delta P_a^* \approx (\rho_0^* U_0^*)^2(1/\rho_{out}^* - 1/\rho_0^*)$, which is proportional to D^{*-2} at a specified inlet Re_0. Since the height of the vertical section is very small, the gravitational pressure drop along the heated section of the pipe is neglected.
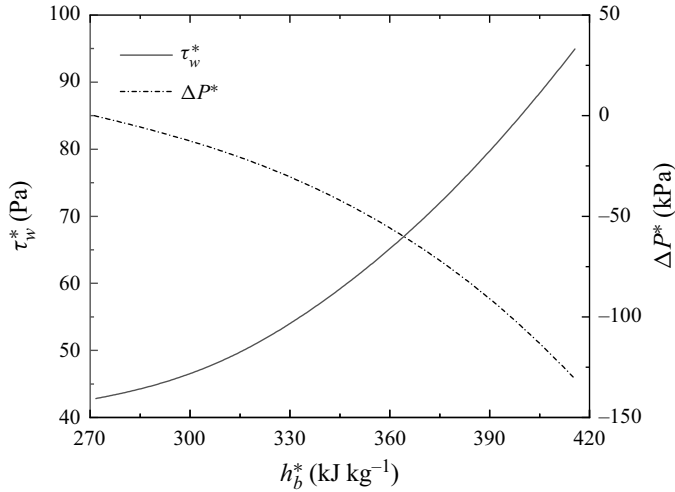
Figure 2. The distribution of the wall shear stress, and the pressure drop along the axial direction of supercritical pressure CO_2 in a micron tube. The diameter of the tube is $D^* = 100\ \mu m$, the inlet pressure is $P_0^* = 7.8\ MPa$, the inlet temperature is $T_0^* = 300\ K$ and the inlet Reynolds number is $Re_0 = 4000$.

Based on the above analysis, the distribution of the wall shear stress and the pressure drop of supercritical pressure CO_2 in a heated tube with diameter $D^* = 100\ \mu m$ are evaluated and shown in figure 2. Setting the inlet pressure to 7.8 MPa, inlet temperature to 300 K and inlet Reynolds number to 4000, the Blasius correlation is used to calculate the friction factor. Since the magnitude of shear stress is inversely proportional to the scale, the dimensional viscous stress in the micron-scale tube with a diameter of $100\ \mu m$ is two orders of magnitude larger than that in tubes with a diameter of 1 mm at the same inlet Reynolds number. Therefore, the pressure drop shown along the axial direction is more than 0.1 MPa, which is remarkable compared with the inlet pressure P_0^*. Figure 3 shows the variation of properties at the pseudocritical temperature with 0.1 MPa pressure drop from $P_0^* = 7.8\ MPa$ and $P_0^* = 8.8\ MPa$. Notably, the physical properties vary significantly with a large pressure drop, especially near $P_0^* = 7.8\ MPa$. From the flow continuity, the following can be deduced:

$$dG = \rho_b du_b + u_b d\rho_b = 0; \qquad (2.5)$$

therefore

$$\frac{du_b}{dx} = -\frac{u_b}{\rho_b}\frac{d\rho_b}{dx} = -\frac{u_b}{\rho_b}\left[\left(\frac{\partial \rho_b}{\partial p}\right)_{T_b}\frac{dp}{dx} + \left(\frac{\partial \rho_b}{\partial T_b}\right)_p\frac{dT_b}{dx}\right]. \qquad (2.6)$$

That is, the flow acceleration includes the part caused by the reduction in pressure along the way and the part caused by the thermal expansion of the fluid. For supercritical pressure fluids flowing in micron-scale diameter channels near the critical point, both parts could have a significant effect on the turbulence dynamics and contribute to severe heat transfer deterioration. Thus, it is necessary to reconsider the pressure variation in the governing equation and thermoproperty update function.

Based on the assumption above, the property change caused by hydrodynamic pressure fluctuations and the viscous heating term is neglected, but the total pressure change term
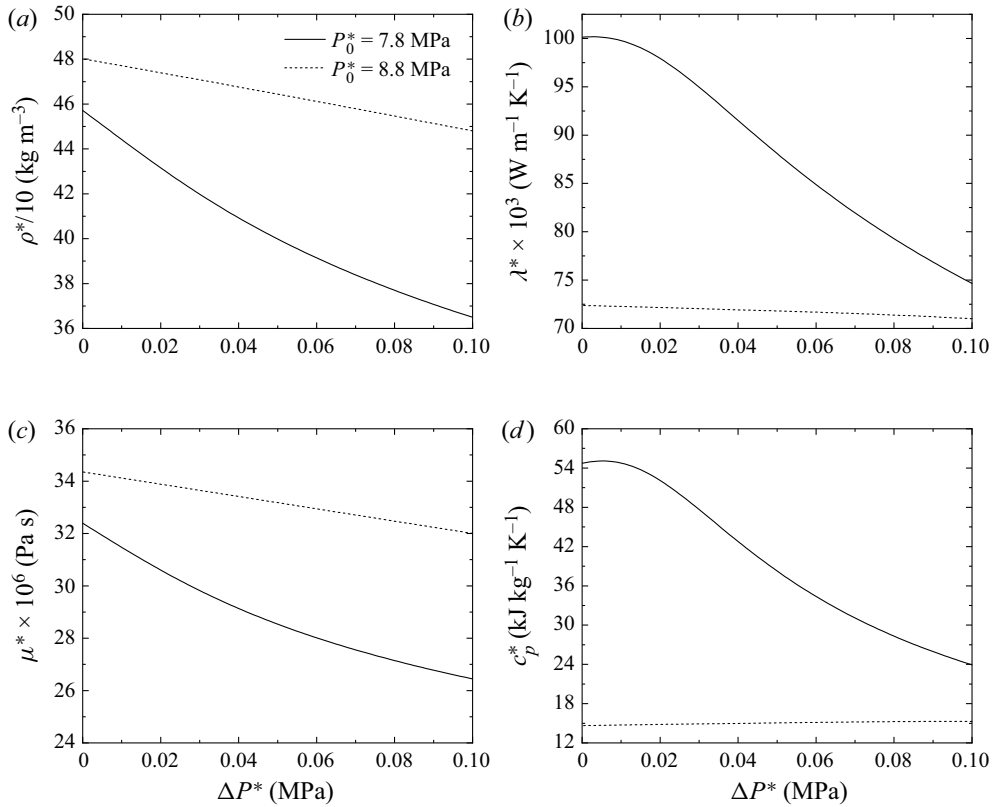
972 A13-8

Figure 3. Variation of the (*a*) density, (*b*) thermal conductivity, (*c*) viscosity, (*d*) specific capacity at T_{pc}^* with 0.1 MPa pressure change from $P_0^* = 7.8$ MPa (—) and $P_0^* = 8.8$ MPa (- -), respectively.

in the governing equations is considered in the micron tube. The governing equations are solved in the following conservation form in a cylindrical coordinate system:

$$\frac{\partial \rho}{\partial t} + \frac{\partial (\rho u_x)}{\partial x} + \frac{1}{r}\frac{\partial (r\rho u_r)}{\partial r} + \frac{1}{r}\frac{\partial (\rho u_\theta)}{\theta} = 0, \tag{2.7}$$

$$\frac{\partial (\rho u_x)}{\partial t} + \frac{\partial (\rho u_x u_x)}{\partial x} + \frac{1}{r}\frac{\partial (r\rho u_r u_x)}{\partial r} + \frac{1}{r}\frac{\partial (\rho u_\theta u_x)}{\partial \theta}$$
$$= -\frac{\partial P}{\partial x} \mp \frac{\rho}{Fr_0^2} + \frac{1}{Re_0}\left(\frac{\partial \tau_{xx}}{\partial x} + \frac{1}{r}\frac{\partial (r\tau_{xr})}{\partial r} + \frac{1}{r}\frac{\partial \tau_{x\theta}}{\partial \theta}\right), \tag{2.8}$$

$$\frac{\partial (\rho u_r)}{\partial t} + \frac{\partial (\rho u_x u_r)}{\partial x} + \frac{1}{r}\frac{\partial (r\rho u_r u_r)}{\partial r} + \frac{1}{r}\frac{\partial (\rho u_\theta u_r)}{\partial \theta} + \frac{\rho u_\theta u_\theta}{r}$$
$$= -\frac{\partial P}{\partial r} + \frac{1}{Re_0}\left(\frac{\partial \tau_{rx}}{\partial x} + \frac{1}{r}\frac{\partial (r\tau_{rr})}{\partial r} + \frac{1}{r}\frac{\partial \tau_{r\theta}}{\partial \theta} - \frac{\tau_{\theta\theta}}{r}\right), \tag{2.9}$$

$$\frac{\partial (\rho u_\theta)}{\partial t} + \frac{\partial (\rho u_x u_\theta)}{\partial x} + \frac{1}{r}\frac{\partial (r\rho u_r u_\theta)}{\partial r} + \frac{1}{r}\frac{\partial (\rho u_\theta u_\theta)}{\partial \theta} + \frac{\rho u_r u_\theta}{r}$$
$$= -\frac{1}{r}\frac{\partial P}{\partial \theta} + \frac{1}{Re_0}\left(\frac{\partial \tau_{\theta x}}{\partial x} + \frac{1}{r^2}\frac{\partial (r^2 \tau_{\theta r})}{\partial r} + \frac{1}{r}\frac{\partial \tau_{\theta\theta}}{\partial \theta}\right), \tag{2.10}$$

972 A13-9

$$\frac{\partial(\rho h)}{\partial t} + \frac{\partial(\rho u_x h)}{\partial x} + \frac{1}{r}\frac{\partial(r\rho u_r h)}{\partial r} + \frac{\partial(\rho u_\theta h)}{\partial \theta}$$

$$= \frac{U_0^2}{c_{p0}T_0}\left(\frac{\partial P}{\partial t} + u_x\frac{\partial P}{\partial x} + \frac{u_r}{r}\frac{\partial P}{\partial r} + \frac{u_\theta}{r}\frac{\partial P}{\partial \theta}\right)$$

$$+ \frac{1}{Re_0}\frac{1}{Pr_0}\left[\frac{\partial}{\partial x}\left(\lambda\frac{\partial T}{\partial x}\right) + \frac{1}{r}\frac{\partial}{\partial r}\left(r\lambda\frac{\partial T}{\partial r}\right) + \frac{1}{r}\frac{\partial}{\partial \theta}\left(\frac{1}{r}\lambda\frac{\partial T}{\partial \theta}\right)\right], \quad (2.11)$$

where

$$\tau_{ij} = 2\mu S_{ij} - \frac{2}{3}\mu\frac{\partial u_k}{\partial x_k}\delta_{ij}, \quad (2.12)$$

$$S_{ij} = \frac{1}{2}\left(\frac{\partial u_i}{\partial x_j} + \frac{\partial u_j}{\partial x_i}\right). \quad (2.13)$$

The negative sign in front of the gravitational force term in (2.8) corresponds to upward flows, and the positive sign corresponds to downward flows. The above governing equations are defined in cylindrical coordinates (x, r, θ) in the present study, where, x, r, θ are the streamwise, radial and circumferential coordinates, respectively. In addition, the wall-normal distance $y(= 1 - r)$ is used in this paper. In the above governing equations, the variables are all in non-dimensional form defined as follows:

$$\left.\begin{array}{c} t = \dfrac{t^*}{R^*/U_0^*}, \quad x_i = \dfrac{x_i^*}{R^*}, \quad u_i = \dfrac{u_i^*}{U_0^*}, \quad P = \dfrac{P^*}{\rho_0^* U_0^{*2}}, \\[3mm] \rho = \dfrac{\rho^*}{\rho_0^*}, \quad \mu = \dfrac{\mu^*}{\mu_0^*}, \quad \lambda = \dfrac{\lambda^*}{\lambda_0^*}, \quad c_p = \dfrac{c_p^*}{c_{p0}^*}, \\[3mm] T = \dfrac{T^*}{T_0^*}, \quad h = \dfrac{h^* - h_{ref}^*}{c_{p0}^* T_0^*}, \end{array}\right\} \quad (2.14)$$

where the subscript 0 denotes the inlet value, and the superscript $*$ denotes a dimensional value. All the equations are in dimensionless form normalized with the inlet bulk velocity denoted by U_0^*, and R^* is the tube radius. The thermophysical properties, including temperature, are normalized by their inlet values. The enthalpy is normalized by the inlet specific heat capacity c_{p0}^*, the inlet temperature T_0^* and the referred enthalpy h_{ref}^*, which is the enthalpy at a temperature much higher than the pseudocritical value at the working pressure. The non-dimensional parameters shown in the governing equations are written as

$$Re_0 = \frac{\rho_0^* U_0^* R^*}{\mu_0^*}, \quad Pr_0 = \frac{\mu_0^* c_{p0}^*}{\lambda_0^*}, \quad \frac{1}{Fr_0} = \frac{g^* R^*}{U_0^{*2}}, \quad (2.15a\text{--}c)$$

where g^* represents the magnitude of the gravitational vector. All the thermophysical properties of CO_2 are from a National Institute of Standards and Technology database (Lemmon, Huber & McLinden 2010). The fluid temperature is calculated first from the computed static enthalpy and thermodynamic pressure, while other properties are updated as functions of temperature and thermodynamic pressure using a third-order spline interpolation along an isobar. Notably, the change in thermodynamic pressure $P^{*(0)}$ is considered when we update the properties.
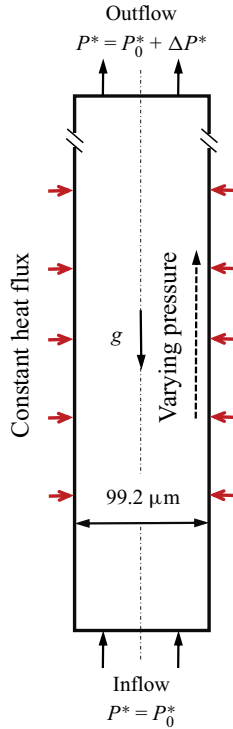
972 A13-10

Figure 4. Schematic diagram of the heated section (for upward pipe flow).

2.2. *Numerical methods*

The low-Mach-number equations for variable-density flows are solved using a conservative space–time discretization scheme that was developed by Pierce (2001), Pierce & Moin (2004) and Wall, Pierce & Moin (2002), in which each velocity component is staggered by half a time step and by half a space step with respect to scalar variables such as temperature and density. An explicit low-storage, third-order Runge–Kutta scheme is used for temporal discretization, while a second-order central difference scheme is used for spatial discretization. The pressure terms in the governing equations are always treated implicitly via the Poisson equation.

The numerical methods described above were previously used to simulate incompressible turbulent flows with variable thermophysical properties at supercritical pressure. The code was successfully validated for velocity profiles and temperature profiles of heated and unheated turbulent flows. The details of their numerical methods and validation can be found in Cao *et al.* (2021), He *et al.* (2021) and Seddighi (2011). The good agreement indicates that the turbulence generator can generate reasonable turbulence in the tube.

2.3. *Simulation conditions*

A schematic diagram of the heated section for upward pipe flow is shown in figure 4. Before the heated section, a periodic inflow turbulence generator with $L^*/R^* = 10$ is applied to generate the time-dependent velocity as inlet boundary condition (Cao *et al.* 2021). The heated section is strongly heated with a constant non-dimensional heat flux,

Case	Type	Flow dir.	P_0^* (MPa)	T_0^* (K)	$2 \times Re_0$	q_w^* (kW m^{-2})	Pr_0	$Bo^* \times 10^9$	$Kv \times 10^7$
A	Vary P	Up	7.8	297.15	2600	130.0	2.75	2.65	5.57
B	Vary P	Up	7.8	297.15	2600	239.0	2.75	4.20	9.65
C	Vary P	Up	7.8	297.15	2600	323.0	2.75	6.01	13.90
C-0	Constant P	Up	7.8	297.15	2600	323.0	2.75	6.01	13.40
I	Vary P	Up	8.8	296.45	3800	259.4	2.44	1.04	4.32
II	Vary P	Up	8.8	296.35	3800	459.6	2.44	1.82	7.37
II-0	Vary P	Down	8.8	296.35	3800	459.6	2.44	1.82	7.37
III	Vary P	Up	8.8	297.55	3800	548.8	2.50	2.42	12.33
III-0	Constant P	Up	8.8	297.55	3800	548.8	2.50	2.03	9.27

Table 1. Flow conditions for the supercritical pressure CO_2 flow simulations ($D^* = 99.2$ μm).

and no-slip boundary conditions at the wall. For the outflow, the convective boundary condition (Orlanski 1976) is specified for the velocities and the enthalpy. The diameter of heated pipe is micron-scale, which is the typical characteristic scale of chamber cooling channels. The significant pressure drop influence and scale effect occurred in the micron-scale pipe. Five experimental cases by Jiang *et al.* (2013) were selected to be simulated using DNS to investigate flow acceleration including thermal expansion and pressure drop acceleration, while the other four cases were selected to simulate flow acceleration considering only thermal expansion in a heated micron tube. Table 1 summarizes the flow conditions in terms of non-dimensional parameters.

The non-dimensional buoyancy parameter Bo^* used to evaluate the buoyancy effect is defined as (Jackson & Hall 1979)

$$Bo^* = \frac{Gr^*}{Re^{3.425}Pr^{0.8}}, \quad Gr^* = \frac{g\alpha_p d_i^4 q_w}{\lambda v^2}. \quad (2.16a,b)$$

The non-dimensional flow acceleration parameter Kv used to evaluate the flow acceleration due to thermal expansion and pressure drop is defined as

$$\left.\begin{array}{l} Kv = \dfrac{v_b}{u_b^2}\dfrac{\mathrm{d}u_b}{\mathrm{d}x} = -\dfrac{d}{Re}\beta_T\dfrac{\mathrm{d}p}{\mathrm{d}x} + \dfrac{4q_w d\alpha_p}{Re^2\mu_b c_p}, \\[3mm] Kv_T = \dfrac{4q_w d\alpha_p}{Re^2\mu_b c_p}, \quad Kv_p = -\dfrac{d}{Re}\beta_T\dfrac{\mathrm{d}p}{\mathrm{d}x}, \end{array}\right\} \quad (2.17)$$

where Kv_T is the non-dimensional thermal expansion acceleration parameter proposed by Mceligot & Jackson (2004) which describes the effect of flow acceleration due to density variation with temperature, and Kv_p is the non-dimensional flow acceleration parameter describing the effect of flow acceleration due to pressure drop through the tube, modified by Jiang *et al.* (2013).

As mentioned in the introduction, when the tube size is reduced to the micron-scale size, the buoyancy effect is reduced; however, the flow acceleration effect, including both the flow acceleration due to thermal expansion and the flow acceleration due to the pressure drop in the tube is more significant than in large tubes. For these cases in simulation, Bo^* has a magnitude of 10^{-9}, much less than the threshold of 5.6×10^{-7} given by Mceligot & Jackson (2004), and 2.0×10^{-7} given by Jiang *et al.* (2010) with buoyancy effects only important for Bo^* above this value. This indicates that the buoyancy effect can be ignored.

972 A13-12

	Case	$Nx \times Ny \times Nz$	Δx^+	Δy^+	Δz^+
Present study	Cases I–III	$3840 \times 56 \times 128$	10.55	0.14–6.33	6.63
Present study	Cases A–C	$3456 \times 72 \times 128$	9.62	0.07–3.37	4.53
Nemati *et al.* (2015)	Initial flow	$512 \times 190 \times 200$	4.47	0.32–2.96	3.13
Abe (2001)	AKM395	$256 \times 192 \times 256$	9.88	0.2–9.64	4.94

Table 2. Details of the mesh used in the present study and comparison with simulations from the literature.
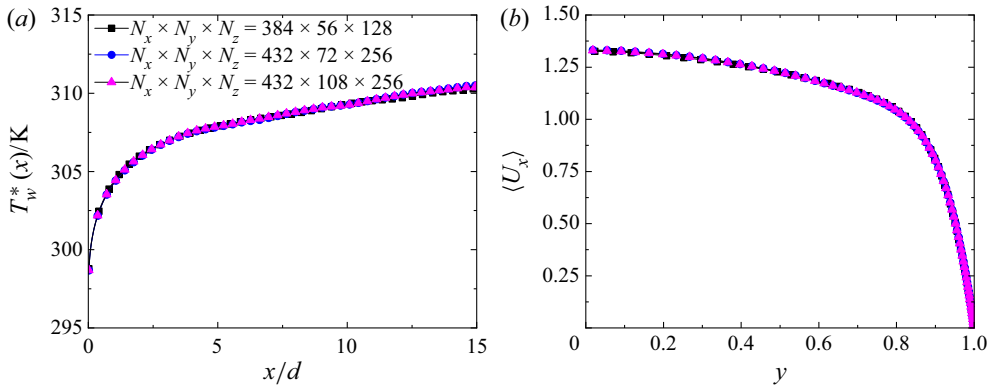
Figure 5. The different mesh resolutions. (*a*) Averaged temperature along the pipe wall for case I. (*b*) Mean axial velocity profile for case I at $x/d = 7.5$. Line, $384 \times 56 \times 128$ (present study); solid symbols, $432 \times 72 \times 256$; hollow symbols, $432 \times 108 \times 256$.

The local non-dimensional flow acceleration parameter Kv has a magnitude of 10^{-7}–10^{-6}, and the previous experiment indicated that the high heat fluxes and the heat transfer were reduced by the flow acceleration effect when the non-dimensional flow acceleration parameter, Kv, exceeded approximately 6.0×10^{-7} (Jiang *et al.* 2013).

The details of the mesh used in the present study and comparison with simulations from the literature are summarized in table 2. In the axial and circumferential directions, the grids are uniform. In the radial direction, the grid spacing is non-uniform with, conveniently, a finer grid spacing near the wall with a hyperbolic tangent function. Note that a grid spacing of approximately $O(0.1\eta)$ and $O(0.1\delta_v)$ in the radial direction is satisfied at the wall, where $\eta \equiv (v^3/\varepsilon)^{1/4}$ is the Kolmogorov scale and $\delta_v \equiv v/u_\tau$ are expected to be smaller than the Kolmogorov length scale η, since the Prandtl number $Pr > 1$. For most of the remaining flow $Pr \approx 4$, and it is believed that the mesh resolution captures all the relevant scales. To quantify this, simulations with two coarser meshes were performed in a short section $L^*/D^* = 10$ for case I in table 2. The results for both meshes are compared in terms of averaged streamwise wall temperatures and axial velocity in figure 5. It can be concluded that a finer mesh would incur a much longer calculation time but make only a slight difference in the results. The difference in the local wall temperature did not exceed ± 0.1 %. Moreover, the mean velocity profiles in the boundary layer proved that the modified code could generate reasonable turbulence in a micron-scale pipe. The non-dimensional time step used was 3.0×10^{-4} while the Courant–Friedrichs–Lewy number (CFL < 1.0) was specified, and the equations were integrated forward in time until the statistically stationary state was reached before collecting turbulence data.

3. Results and discussion

The purpose of the present study is to further understand the mechanism of turbulent convective heat transfer of supercritical pressure fluids in heated microtubes, which is influenced by variations in thermophysical properties, the scale effect and flow acceleration; the last two factors are particularly significant in micron-scale tubes. In this discussion, we first give a comparison between DNS and experiments and the analyse the heat transfer and flow characteristics both qualitatively and quantitatively. Next, we investigate the thermophysical property variations with respect to the temperature and pressure changes, and their influence on turbulent motions and convective heat transfer. Subsequently, we investigate instantaneous and mean velocity fields to show the development of the original turbulence in the spatial accelerating flow. This is followed by a discussion on the development of turbulence statistics and structures. To that end, we elucidate the physical mechanism of the peculiar characteristics of turbulent heat transfer to supercritical pressure fluids in a heated micron tube.

In the results and discussion, the mean quantities are obtained by taking a statistical average over time and the homogeneous circumferential direction using Reynolds and Favre averaging. In the following discussions, Favre averaging and Reynolds averaging are used to obtain the mean quantities of density-variable turbulent flows. Let φ be a general property of turbulence that can be decomposed into the Reynolds form or Favre form. The Favre average is defined as

$$\tilde{\varphi} = \overline{\rho\varphi}/\bar{\rho}\varphi = \tilde{\varphi} + \varphi'', \tag{3.1}$$

where $\bar{\varphi}$ denotes the Reynolds average, which is defined as an average over time and the homogeneous circumferential direction. For the steady state conditions studied in this study, a sufficiently long period of time after full development is selected to be statistically averaged to give direct statistical values of Reynolds stress and other parameters for the observation and analysis of turbulence behaviour. Notably, the mean temperature is always calculated with Reynolds averaging.

3.1. *Heat transfer and hydraulic resistance characteristics*

In this section, we begin the investigation with the heat transfer and hydraulic resistance characteristics of the present simulations and compare the results of DNSs and experiments. The corresponding experimental studies were conducted by the authors' group (Jiang *et al.* 2013) using a vertical smooth stainless steel 1Cr18N9T tube. The inner tube diameter was 99.2 µm and the outer diameter was 217 µm. The test section had a 40 mm heated section and 5 mm adiabatic sections before and after the heated section. The authors indicated that the experimental uncertainty of the heat transfer coefficient was ±12.7 %, and the experimental uncertainty of the pressure was 0.13 %. Since the effects of the flow acceleration are more significant at relatively lower pressures close to pseudocritical point and lower inlet Reynolds number, in the simulation the boundary conditions of cases A–C were set to be consistent with the relatively low inlet pressure and low Reynolds numbers cases of the experimental studies. In this way, we were able to provide comparisons of the wall temperature, Nusselt number and pressure drop between the DNS and experimental results.

In the discussion, we need to define some of the physical quantities in the experiments and simulations. The local heat transfer coefficient, h_x^*, at each axial location is calculated as

$$h_x^* = \frac{q_w^*(x)}{T_w^*(x) - T_b^*(x)}, \tag{3.2}$$

where $q_w^*(x)$ is the local heat flux on the inner wall, $T_w^*(x)$ is the inner wall temperature and $T_b^*(x)$ is the local bulk fluid temperature. Based on the mass and energy conservation, the bulk parameters are defined as follows:

bulk mass flux, G_b^*,

$$G_b^* = \frac{1}{A} \int_A \overline{\rho u_x} \, \mathrm{d}A; \tag{3.3}$$

bulk enthalpy, H_b^*,

$$H_b^* = \frac{1}{G_b^* A} \int_A \overline{\rho u_x h} \, \mathrm{d}A; \tag{3.4}$$

bulk temperature, T_b^*, and bulk thermophysical property, ϕ_b^*,

$$T_b^* = T(P^{*(0)}, H_b^*)/T_0^*, \quad \phi_b^* = \phi(P^{*(0)}, T_b^*)/\phi_0^*; \tag{3.5a,b}$$

bulk velocity, U_b^*,

$$U_b^* = \frac{G_b^*}{\rho_b^*} \tag{3.6}$$

the convective heat transfer coefficient, h,

$$h = \frac{q_w^*}{T_w^* - T_b^*}. \tag{3.7}$$

The streamwise distributions of the dimensional wall temperature T_w^* and local Nusselt number $Nu(x)$ are shown in figure 6(a,b). In figure 6(a), the DNS results for the relatively low pressure and low inlet Reynolds number cases A–C show trends similar to those of the corresponding experimental measurements with a local peak and then a decline, which indicates that the heat transfer decreases locally. Figure 6(b) gives the distributions of wall temperature at 8.8 MPa. For case I, the heat flux is low and the bulk temperature at outflow is beyond pseudocritical temperature. The wall temperature distribution is almost linear after the entrance region, which represented the normal heat transfer behaviour of supercritical pressure fluids. With the increase of heat flux, the distribution of wall temperature shows a non-monotonic trend. This local heat transfer decrease is due to the continuously reduced turbulence while accelerating along the streamwise direction, as shown below. When the bulk fluid temperature approaches T_{pc}^*, all of the thermal properties change dramatically, and the large variation in the other thermophysical properties obviously introduce complexity to the heat transfer. In particular, the significant density change associated with a large flow acceleration is expected to occur in the axial direction. In regions farther downstream, $T_w^*(x)$ begins to decrease along the streamwise direction after reaching a peak, which is also observed in the convection heat transfer under the influence of buoyancy effect. However, it is noticed that the locations of the wall temperature peaks due to flow acceleration barely change as with the heat flux increased.

Figure 6(c,d) show the distributions of the corresponding local $Nu(x) = h^* D^* / \lambda_b^*$, where h^* is the convective heat transfer coefficient, D^* is the diameter of the tube and λ_b^* is the bulk thermal conductivity. In figure 6(c), the comparison of the Nusselt number between the present DNS results and experimental results is presented. Quantitatively, the predictions of the integral heat transfer parameter, including the wall temperature and the local Nusselt number, are in good agreement with the experimental data. The maximum absolute errors in T_w and Nu between experiments and predictions are 5.80 K and 14.22. Neglecting the possible inconsistency in boundary conditions, the DNS code was proven to
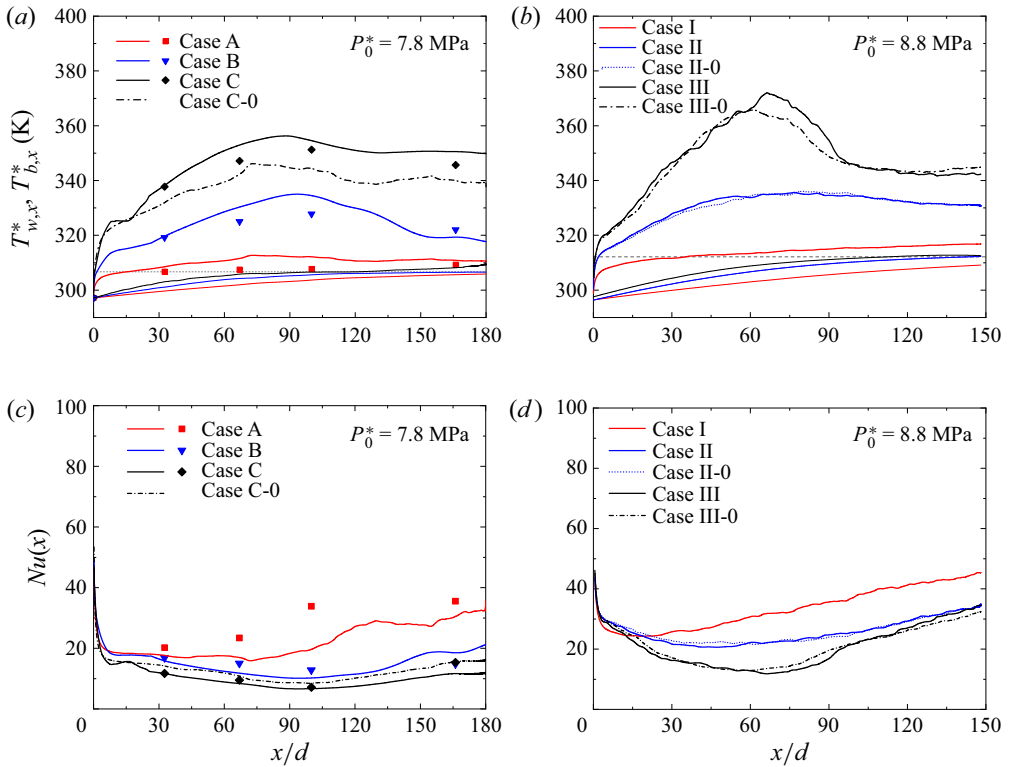
Figure 6. Streamwise distributions of wall and bulk temperature (*a*,*b*), and the local Nusselt number $Nu(x)$ (*c*,*d*). Thin lines for bulk fluid temperature T_b^* for both experiments and simulations, thick lines for DNS results, symbols for experimental results.

produce good results for heat transfer of supercritical pressure fluids in the heated micron tubes. The magnitude of $Nu(x)$ directly represents the strength of convective heat transfer capacity. As already explained in the temperature behaviours, for lightly accelerating case I the local Nusselt number $Nu(x)$ increases monotonously, for significantly accelerating cases A–C and II–III the local Nusselt number $Nu(x)$ decreases at first and then increases along the streamwise direction.

Because the Bo^* number and Kv number based on the bulk properties are independent of the flow direction, only one value for the upward direction is given in the following analysis. Figure 7 shows the distribution of the local Bo^* number and the local Kv number for upward flow. As shown in figure 7(*a*,*b*), the Bo^* number is higher near the inlet and then decreases rapidly. The peak Bo^* in this set of conditions is much less than the critical value of 2.0×10^{-7} proposed by Jiang *et al.* (2010). This indicates that the effect of the buoyancy force is negligible for all cases in our simulation.

The distributions of the dimensionless factors Kv_T and Kv_p characterizing the fluid acceleration effect due to thermal expansion and pressure drop are given in figure 7(*c*,*d*). The distribution pattern at low inlet Reynolds number is consistent with that at high inlet Reynolds number. Also, Kv_T increases with increasing heat flow density, peaks at fluid temperature close to quasicritical temperature and then decreases, and at high heat flow density, the value of Kv_T is already greater than the value of the threshold value 6.0×10^{-7} (Jiang *et al.* 2013). Then Kv_p increases with increasing fluid temperature, peaks
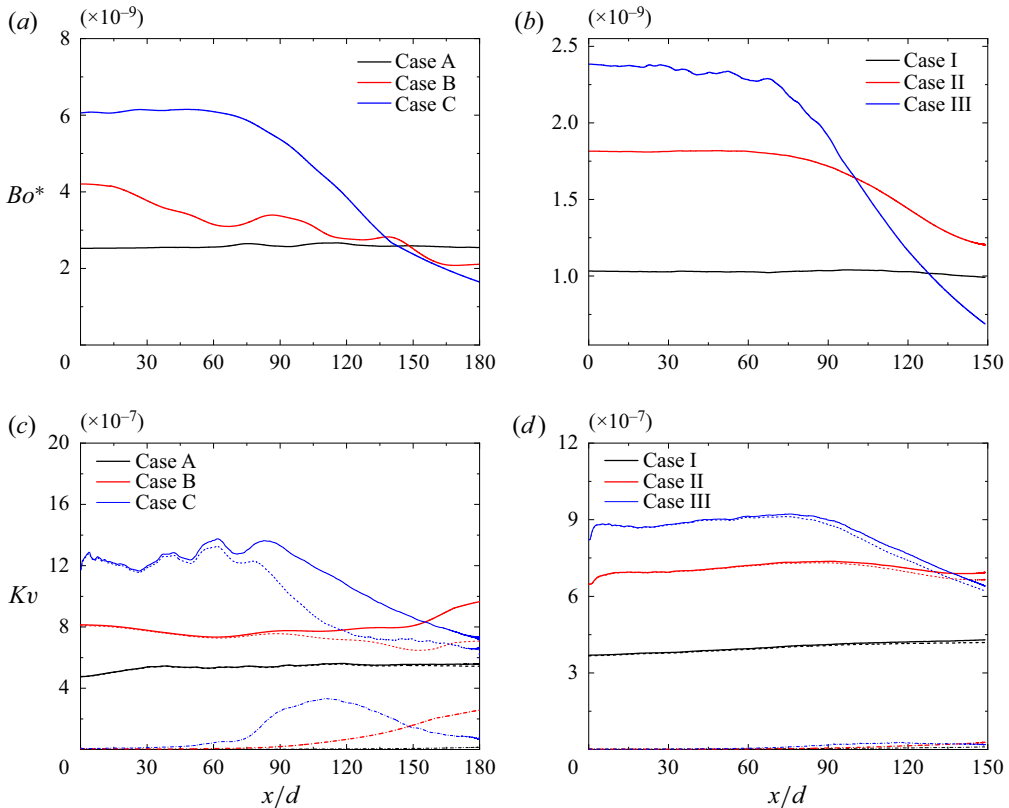
972 A13-16

Figure 7. Streamwise distributions of the buoyancy parameter Bo^* (a,b) and the flow acceleration parameter Kv (lines, —), Kv_T (dash lines, - -) and Kv_p (dash dot lines, -·-) (c,d).

when the fluid temperature approaches the quasicritical temperature and then decreases rapidly. The trend of the distribution of Kv is similar to that of the dimensionless factor Kv_T. Comparing Kv_T and Kv_p values, Kv_p is relatively low, but the magnitude of the Kv_p value is the same as that of Kv_T in cases A–C at relatively low inlet pressure and Reynolds number. The distribution of Kv values is improved by the Kv_p value as shown in figure 7(c). Therefore, the contribution of Kv_p to Kv is not negligible for case A–C, and Kv_p causes a backwards shift in the location where the peak Kv appears, and thus the Kv peak appears exactly at the location of the peak wall temperature. For the cases I–III at relatively high inlet pressures and Reynolds numbers, the convection heat transfer is expected to be influenced by only thermal expansion since Kv_p is one order of magnitude less than Kv_T.

Comparing figure 6 with 7, the position of the maximum local Kv number is close to the position of the minimum local Nu number, and the two trends are opposite. The flow acceleration changes the mean velocity distribution of the fluid cross-section, and the decrease of the flow acceleration is stronger than the buoyancy force in the downward flow, resulting in the weakening of the turbulent shear stress near the wall and the suppression of turbulent kinetic energy generation.

The distributions of the local Nusselt number Nu_f show that the convection heat transfer for the relatively high heat flows is severely impaired and then recovered in the heated micron-scale tubes due to the flow acceleration. It is interesting to compare the present
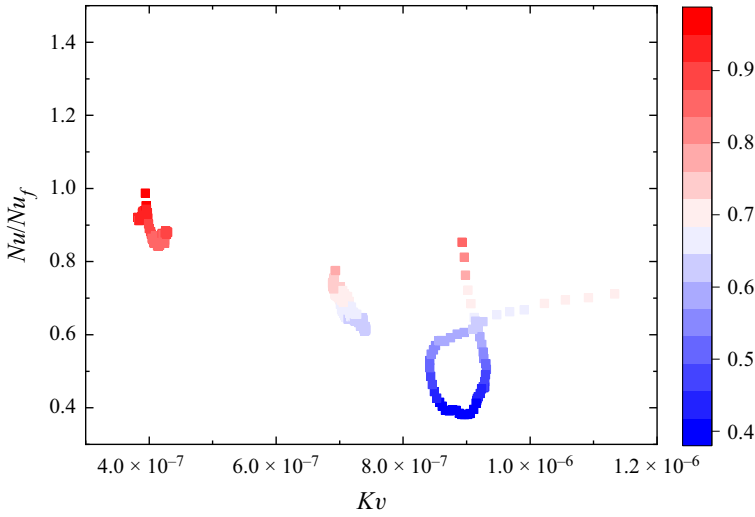
Figure 8. Distributions of the Nusselt number radios with Kv number.

Nusselt number with that of forced convection. In figure 8, the ratios of the local Nusselt number for mixed convection Nu to that of forced convection Nu_f are plotted in terms of the flow acceleration parameter Kv. Here Nu_f is obtained from the modified Krasnoschekow & Protopopov correlation by (Jackson & Hall 1979)

$$Nu_f = 0.0183 Re_b^{0.82} Pr_b^{0.4} \left(\frac{\rho_w^*}{\rho_b^*} \right)^{0.3} \left(\frac{\overline{c_p^*}}{c_{pb}^*} \right)^n,$$ (3.8)

where the exponent n for $(\overline{c_p^*}/c_{pb}^*)^n$ is defined as

$$n = \begin{cases} 0.4, & \text{for } T_b^* < T_w^* \leq T_{pc}^* \text{ or } 1.2 T_{pc}^* \leq T_b^* < T_w^*, \\ 0.4 + 0.2 \left(\dfrac{T_w^*}{T_{pc}^*} - 1 \right), & \text{for } T_b^* \leq T_{pc}^* < T_w^*, \\ 0.4 + 0.2 \left(\dfrac{T_w^*}{T_{pc}^*} - 1 \right) \\ \quad \times \left[1 - 5 \left(\dfrac{T_w^*}{T_{pc}^*} - 1 \right) \right], & \text{for } T_{pc}^* < T_b^* \leq 1.2 T_{pc}^* \text{ and } T_b^* < T_w^*. \end{cases}$$ (3.9)

Note that $\overline{c_p^*} = (1/T_w^* - T_b^*) \int_{T_b^*}^{T_w^*} c_p^* \, dT = (h_w^* - h_b^*)/(T_w^* - T_b^*)$. The correlation was proposed based on supercritical CO_2 experiments data at P, 7.8–9.8 MPa; Re, 8×10^4–5×10^5; $q_w \leq 260$ kW m^{-2}; d, 4.1 mm. The normalized Nusselt numbers in the present simulations decreases as the Kv number increased and is less than unity when Kv exceeds 6.0×10^{-7} (see figure 8). The results are in excellent agreement with the experimental conclusion.

The hydraulic resistance characteristics of cases A–C and I–III are shown in figure 9. Figure 9(a) shows the streamwise distributions of the bulk Reynolds number Re_b. Due to the increase in fluid temperature, which is influenced by the decreases in density and viscosity, along the flow direction, the fluid accelerates very significantly, and the Re_b
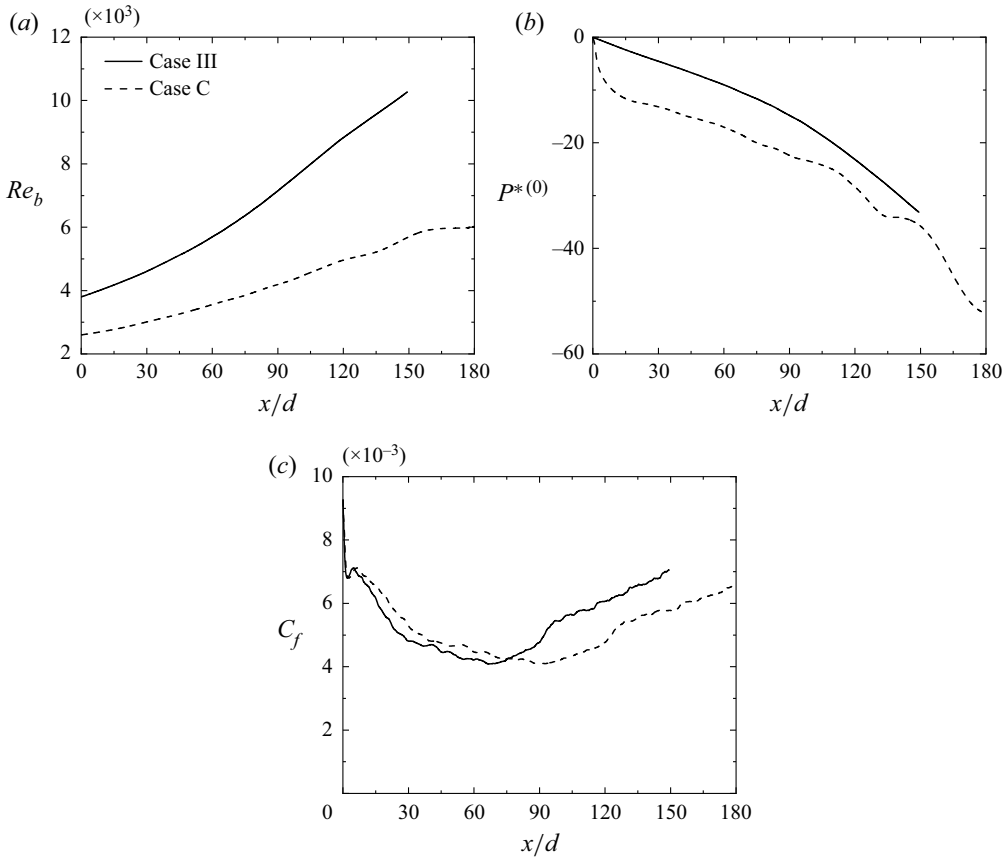
972 A13-18

Figure 9. Streamwise distributions of Reynolds number, pressure drop, and the local friction coefficient for case B and III: (a) Re_b, (b) $P^{*(0)}$ and (c) C_f.

number increases rapidly. The effect of streamwise flow acceleration is coincident with the Kv number shown in figure 8. This fact implies that the effect of bulk flow acceleration on the change in heat transfer characteristics is significant in the present simulations.

Distributions of dimensional pressure drops along the streamwise direction are shown in figure 9(b). In the low heat flux case I, the distribution of $P^{*(0)}$ is almost linear because the average wall shear stress is basically unchanged. As the wall heat flux increases for case II, the temperature of the near-wall fluid increases at the inlet region, which causes sudden reductions in the dynamic viscosity and wall shear stress near the wall. Therefore, the gradient of the axial pressure drop at the inlet region decreases at first due to the variable viscosity. However, as the flow temperature is heated beyond the pseudocritical point T_{pc}^* in the flow downstream, the significant density gradient contributes to the great flow acceleration associated with both increasing friction pressure drop ΔP_f^* and increasing acceleration pressure drop ΔP_a^*. As the flow acceleration effect increases further, such as in cases A–C, the pressure drops become considerably larger than those in cases I–III and the gradient of the pressure drops continue to increase along the downstream direction. Additionally, the overall pressure change from the inlet to the exit increases as the wall heat flux increases, and is not negligible compared with the inlet thermodynamic pressure
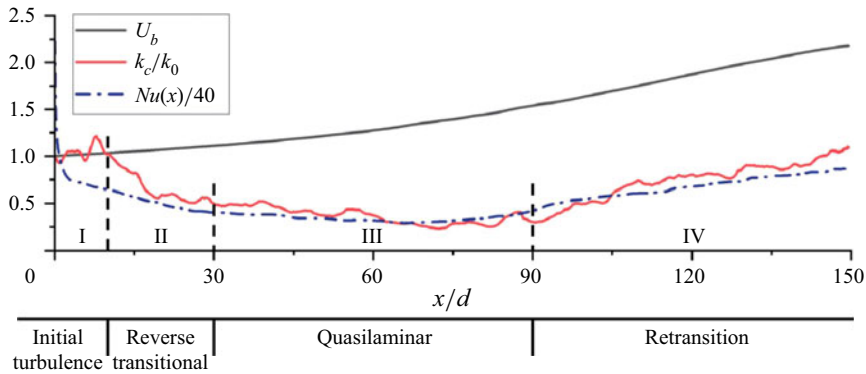
Figure 10. Diagram of the flow situation considered, with a preliminary division into different stages.

$P^{*(0)}$; this is consistent with the modified low-Mach-number assumption adopted in the present study.

Distributions of the local skin friction coefficient compared with the Blasius correlation are shown in figure 9(*c*). For cases I to III, where the flow acceleration is mainly caused by thermal expansion, C_f decreases slightly near the inlet due to the reduction in dynamic viscosity, which is in agreement with the distribution of pressure drops. For case II, the reduction in C_f near the inlet is end at approximately $x/d = 30$, and subsequently increased because of a steeper mean velocity gradient near the wall due to flow acceleration in the streamwise direction. For case C, where the flow acceleration effect is strongest among all the cases considered, a quick increase in C_f is observed from the inlet. The local skin friction coefficient at the downstream region varies significantly, which indicates that the turbulence dynamic is significantly affected by the flow acceleration and the various properties in the micron-scale tube.

Undoubtedly, the developing turbulence due to acceleration is strongly associated with heat transfer and hydraulic resistance characteristics. Studying the mechanism of such turbulence development has not only academic significance but also great practical engineering value. Thus, we proceeded to make a diagram of the different stages of the flow. Figure 10 illustrates a framework for the present analysis of the typical simulation. The initial turbulence at the inlet $x/d = 0$ is fully developed by a turbulence generator with periodic boundary conditions. Beyond that, a steep velocity gradient is formed by flow acceleration. It is reasonable to begin by dividing region I in the neighbourhood of the inlet, believing that the flow in this region still remains turbulent, similar to the initial turbulence. Region II is defined as a transitional region, where the turbulence kinetic energy continues to decrease. Region III far downstream represents the completion of the reversion, which is identified by specifying the degree to which the Reynolds stresses are negligible. In this region, the velocity fluctuations inherited from the previous history may have remained, but no new vortical structures are generated, which in such circumstances could be claimed that to have reached a quasilaminar state. Finally, in region IV, retransition occurs in the high Reynolds flow. This framework provides an overall picture of the development process that largely describes the simulation observations of the acceleration turbulence at supercritical pressure. A more quantitative and detailed investigation is conducted based on the specific physical mechanisms in these regions.
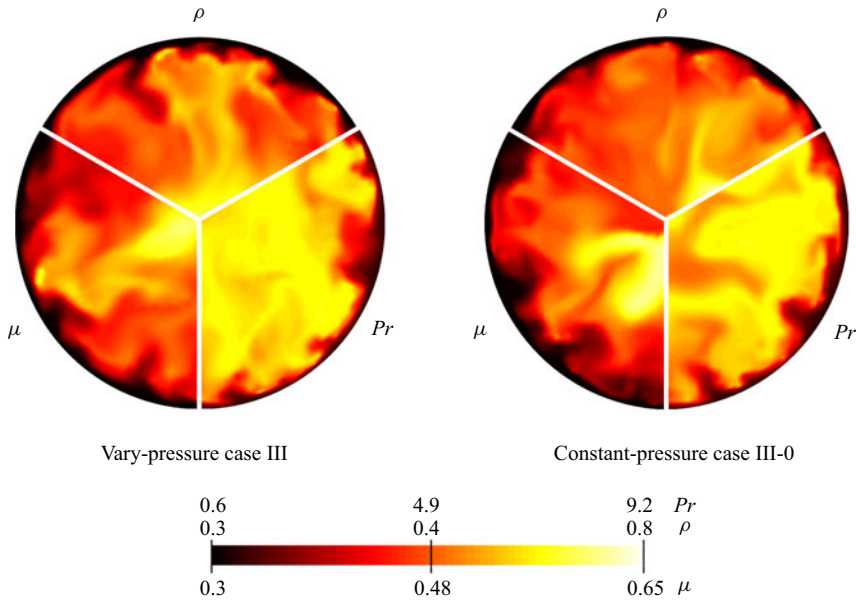
972 A13-20

Figure 11. Instantaneous values of thermophysical properties for case III (Vary-pressure, left) and case III-0 (Constant pressure, right) at the location where $h_b^* = 3.435 \times 10^5$ (h_{pc}^* at 8.8 MPa). The upper third shows the density, the lower left shows the dynamic viscosity and the lower right shows the Prandtl number.

3.2. *Statistics of thermophysical properties*

The analysis in the previous section shows that for heat transfer by turbulent convection of a fluid at supercritical pressure in a heated micron tube, the pressure drop along the streamwise direction is significant. The effect of the pressure drop has a key role in terms of heat transfer and turbulent dynamics, referred to as both a direct effect in the governing equations and an indirect effect on the thermophysical properties. Since the pressure drop driven flow acceleration in high inlet Reynolds number cases I–III could approximately be ignored according to § 2.1, cases I–III considering the pressure change as well as the contrast case III-0 with constant pressure were selected to analyse the thermophysical property influence.

In the simulation cases, the fluid was heated by the wall heat flux, and the fluid in the near wall region was rapidly heated above the pseudocritical temperature. Thus, the fluid density and viscosity were reduced significantly, and the Prandtl number and specific heat capacity of the fluid peaked near the pseudocritical temperature. Figure 11 shows the instantaneous distributions of the Prandtl number, density and dynamic viscosity in the varied pressure case III and constant pressure case III-0. Drastic variations in thermophysical property values are observed in the cross-section. Along the radial direction, the low-density/low-dynamic-viscosity fluid and the high-density/high-dynamic-viscosity fluid mixes strongly, which indicates the significant turbulent motion near the wall. Moreover, the low-density area in case III is larger and more fully blended than in case III-0 considering the pressure change influence on the property, which is quantitatively analysed in figure 12.

The distributions of the mean density, dynamic viscosity, specific heat capacity and Prandtl number for cases I, III and III-0 are shown in figure 12. The radial profiles of the density show that the density changes little along the flow direction for the low heat
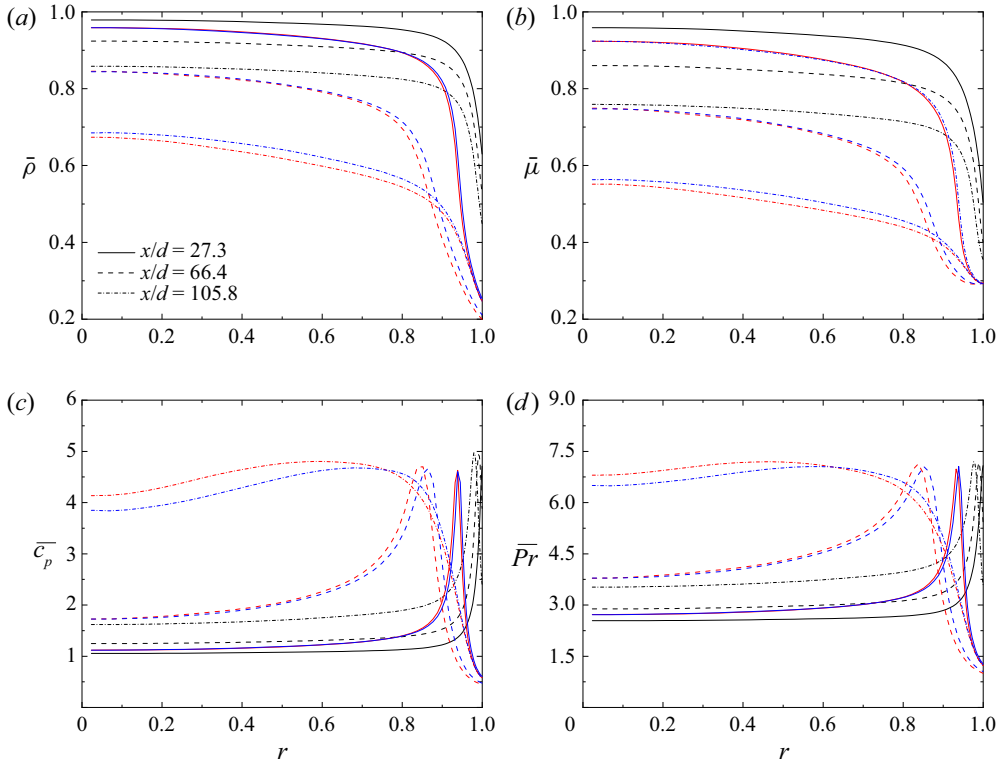
Figure 12. Radial profiles of mean thermophysical properties for vary-pressure cases and constant pressure cases. Black and red lines indicate results from vary-pressure cases I and III, respectively. Blue lines indicate results from constant pressure case III-0.

flux for case I. As the heat flux increases, the enthalpy difference along the flow direction increases; therefore, a significant density difference is observed in the axial coordinate. The three axial locations shown are equally spaced; $x/d = 66.4$ is the location where the heat transfer coefficient achieves the lowest value (see figure 7), and $x/d = 105.8$ is the location where the bulk enthalpy H_b^* achieves $H_{b,pc}^*$. According to the energy conservation law, for the same energy input, the enthalpy increase of supercritical pressure CO_2 in cases III and III-0 are the same. Therefore, as shown in figure 7, with the same local enthalpy, there is an obvious difference in the thermophysical properties in cases with variable and constant pressure. This indicates that the property variation with pressure change is non-negligible, i.e. the density variation is

$$d\rho = \left. \frac{\partial \rho}{\partial P} \right|_T dP + \left. \frac{\partial \rho}{\partial T} \right|_P dT, \tag{3.10}$$

where P denotes the thermodynamic pressure $P^{*(0)}$, and T denotes thermodynamic temperature. From figure 10 we can see that dP along the axial direction is non-negligible. The results verifies the assumption that the effect of pressure variation on the physical properties inside the micron tube could not be neglected. Due to the effect of the pressure drop along the flow direction, there is a difference between the local density and the local dynamic viscosity at the same enthalpy value, especially at the location where the fluid temperature crosses the pseudocritical temperature near the wall. The lower the pressure
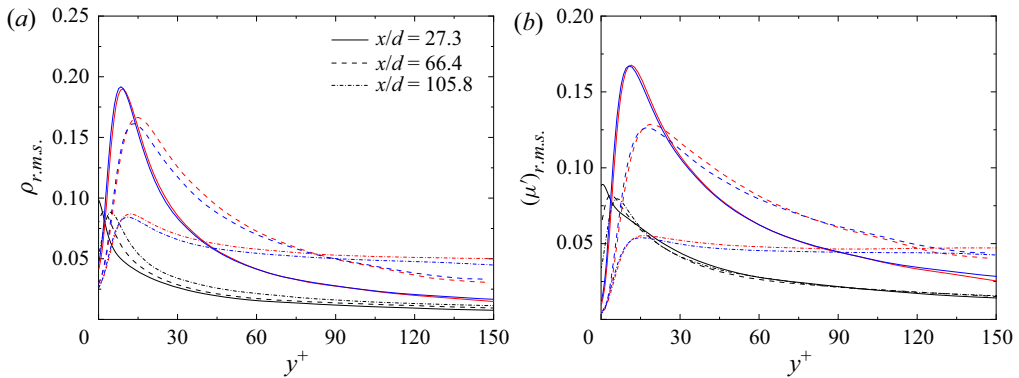
972 A13-22

Figure 13. Root-mean-square profiles of property fluctuations in cases I, III and III-0. Black and red lines indicate results from vary-pressure cases I and III, respectively. Blue lines indicate results from constant pressure case III-0.

is, the lower the values of density and dynamic viscosity at the same local location, while the peak of specific heat capacity and Prandtl number moves towards the centre of the tube. Along the direction of flow, the pressure difference becomes larger, which in turn leads to a larger difference in physical properties.

Figure 13(a,b) shows the root-mean-square (r.m.s.) profiles of the density and dynamic viscosity fluctuations. The fluctuations presented in the high heat flux cases are found to be much larger than those in the low heat flux case. At the upstream location $x/d = 22.7$, the largest normalized thermophysical property fluctuation intensity is 20 % for density $\rho_{r.m.s.}/\bar{\rho}$ and 18 % for dynamic viscosity $\mu_{r.m.s.}/\bar{\mu}$ for high heat flux case III. For low heat flux case I, the largest value of $\rho_{r.m.s.}/\bar{\rho}$ is 10 % while that of $\mu_{r.m.s.}/\bar{\mu}$ is 9 %, and the largest thermophysical property fluctuation intensities are almost unchanged along the flow direction. This is because for the low heat flux case, the pseudocritical point is always located in the laminar layer where the turbulence fluctuation is weak. However, for cases with large heat flux, the pseudocritical point moves towards the centre flow region, and the large values of the molecular Prandtl in the buffer layer as well as in the centre region with strong turbulence fluctuation contribute to locally more significant thermophysical property fluctuations. When the fluid temperature exceeds the pseudocritical temperature at $x/d = 105.8$, the molecular Prandtl number decreases and thus, the fluctuation of the physical properties becomes weaker again. The difference in fluctuation intensities at the same location between cases III and III-0 could be attributed to the change in the local molecular Prandtl number with the pressure drop.

The local steep pressure gradients lead to locally steep thermophysical property gradients, such as density and dynamic viscosity, as shown in figure 14(a,b). The difference between the bulk properties observed only is apparent while the pressure drop is significant downstream. The bulk density gradient as well as the local density gradient affects flow acceleration. The distorted profiles of the velocity field and the dynamic viscosity variation influences the turbulence shear stress and turbulence structures, thereby affecting turbulence production. The distributions of thermophysical properties in cases A–C are similar to those discussed for cases I–III.

The thermophysical properties of the near-wall region have a direct or indirect effect on the generation of turbulence and the thickness of the thermal boundary layer. The direct effect refers to the influence on the heat transfer and turbulence production due
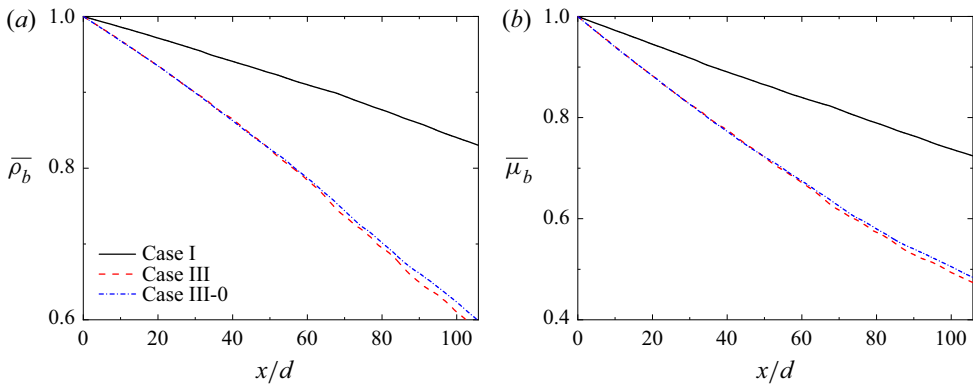
Figure 14. Distributions of mean bulk thermophysical properties along the axial direction for vary-pressure cases and constant pressure cases. Black and red lines indicate results from vary-pressure cases I and III, respectively. Blue lines indicate results from constant pressure case III-0.

to thermophysical property fluctuations. For example, the peak value of the specific heat capacity contributes to the strong ability of fluids to carry heat. The density and dynamic viscosity are also explicitly included in the expression of turbulent statistics, such as turbulence shear stress $\overline{\rho u_x'' u_r''}$ and viscous shear stress $\bar{\mu} \partial u_x / \partial r$. The variations in thermophysical properties directly influences the turbulence statistics. However, the indirect effect of thermophysical properties refers to the indirect consequences of the mean velocity profile caused by local flow acceleration or deceleration. The decrease in density or increase in dynamic viscosity along the flow direction aids the flow such that the profiles of the velocity field is distorted and thereby changes the gradient of the velocity, which is also called flow acceleration.

In the previous discussion, we compared the distributions of the mean profiles as well as the fluctuation profiles of the thermophysical properties for vary-pressure cases III and constant pressure III-0. Since the flow acceleration driven by the pressure drop was not significant in the corresponding inlet pressure and Reynolds number, it was concluded that the influence of pressure change considered was essentially presented in the reflected values of physical properties. Figure 15 shows the distributions of the mean local wall temperature and the local Nusselt number for cases III and III-0. For the case considering the pressure drop, the worst deteriorated point of flow heat transfer moves downstream, and the peak wall temperature is higher. However, the subsequent heat transfer recovery in case III is better than that in case III-0 after $x/d = 100$. The observation is attributed to the direct and indirect effects of thermophysical property variation due to the pressure change, as discussed in the following section.

3.3. *Mean and instantaneous velocity fields*

In this section, we discuss how the pressure change, thermophysical property variation and flow acceleration effects modulate turbulent flow. The changes in flow patterns under the acceleration of flows at supercritical pressure flows were investigated for both mean and instantaneous velocity fields. An apparent streamwise speed increase is found in the mean streamwise velocity profiles owing to the significant density gradient in both the centre and near-wall regions. For cases with low or high inlet Reynolds numbers, the flow acceleration attributes of the velocity profiles are flat and increase in magnitude, when compared with the velocity profile of the inlet flow. This is a consequence of density fluctuations due to the
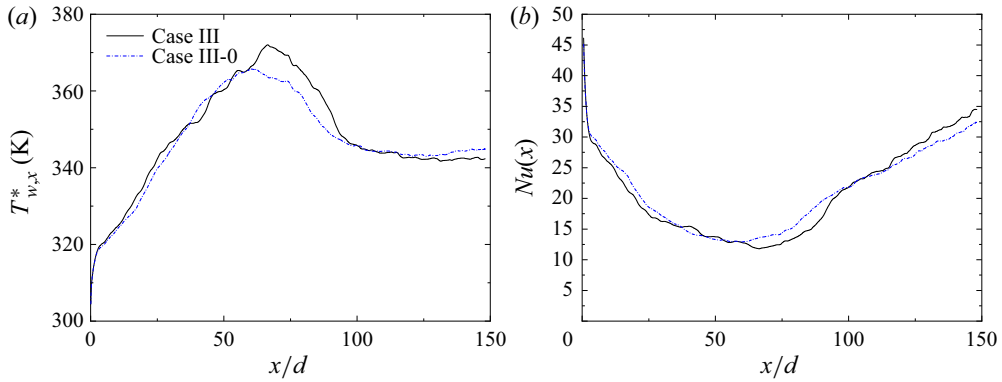
972 A13-24

Figure 15. Radial profiles of (*a*) the mean local wall temperature and (*b*) the local Nusselt number distributions along the axial direction for cases III and III-0.
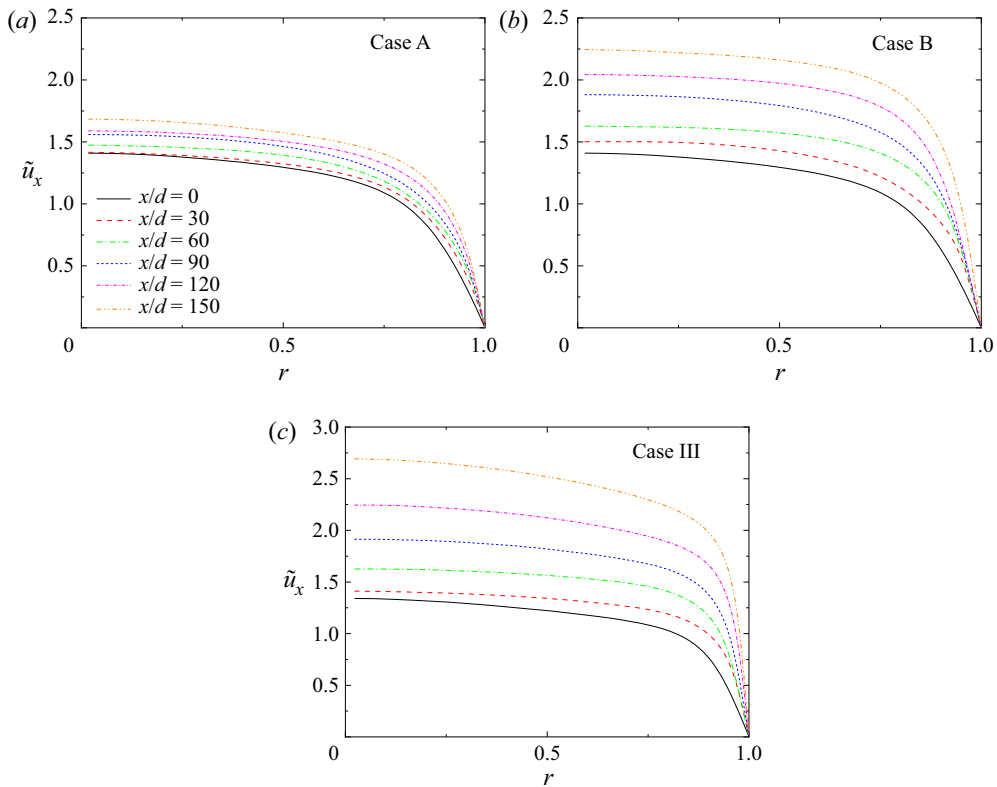

Figure 16. Radial profiles of the mean streamwise velocity for cases A, B and III at different axial locations.

streamwise enthalpy increase across the pseudocritical point. The significant density drop in the bulk of flow causes bulk flow acceleration rather than local flow acceleration (see figure 16) in the near-wall region, which is in stark contrast to that due to the buoyancy effect. Notably, the mean strain rates $\partial \overline{u_x}/\partial r$ at the hot wall increases, while that in the centre flow region decreases during the initial acceleration phase.

The instantaneous distributions of fluctuating velocities in both axial and wall-normal directions are presented in figure 17 across a spanwise span at $y^+ = 19$ for cases A, B and III. For the former two cases, the inlet Reynolds number based on the tube diameter is 2600. In these two cases, a typical characteristic of low Reynolds number turbulent flow is observed at the inlet, where the contours of the streamwise fluctuating velocity shows random fluctuations with some weak streaky structures. As the flows accelerated along the streamwise direction, the streamwise velocity fluctuation is strengthened and forms more high- and low-speed streaks, which is similar to the boundary layer bypass transition processes from laminar flows. In the downstream, some isolated turbulent spots are observed in the accelerated flow after $x/d = 120$, and in case B, the turbulence spots gradually fills the entire flow region similar to fully developed turbulence. In case III, the inlet Reynolds number is 3800, and the streamwise velocity fluctuations are generally stronger than those in low Reynolds number flows. Likely, the development of streamwise fluctuating velocities is continuedly enhanced in case III, and the turbulence intensity is significantly higher in the downstream than in the inlet.

Figure 17(*b*) illustrates the development of the wall-normal velocity fluctuations along the flow direction. Unlike the streamwise velocity, the wall-normal velocity undergoes a process of decay followed by regeneration. For relatively low inlet Reynolds number cases A and B, the radial turbulent fluctuations almost disappear after the inlet development section. The 'silent' flow pattern continued until $x/d = 120$, and many turbulence spots appear abruptly when passing the monitoring line. In case III, a similar attenuation is observed in that the fluctuations of wall-normal velocity are relatively weak compared with those before $x/d = 10$ and after $x/d = 90$. This behaviour is related to changes in the turbulent kinetic energies and coherent structures during strong flow acceleration along the streamwise direction, indicating that the initial turbulence attenuation and regeneration.

The development of turbulent flow observed here is seen as a modulation of the flow acceleration for the initial turbulence. Streamwise velocity fluctuations are always present due to the significant mean velocity gradient in the axial direction and eventually lead to stronger turbulence in the high-speed flow downstream. Intriguingly, during the transition process, the wall-normal and spanwise (not shown here) fluctuating velocities significantly decline, which indicate that the streamwise vorticity might have disappeared during the modulation of streamwise acceleration.

Figure 18 shows the r.m.s. profiles of the streamwise and wall-normal velocity fluctuations. For case A, the wall heat flux is small, so the streamwise flow acceleration shown in figure 16(*a*) is not great. However, the wall-normal fluctuating velocities in the vicinity of the wall are enhanced after a period of decay, in agreement with the visualization in figure 18(*b*). As the heat flux increases, the pressure and temperature change of the bulk flow in case B are larger and lead to more significant flow acceleration. In comparison with u_x'' in case A, the fluctuation decay is more severe in case B, but significant turbulence regeneration is observed after $x/d = 150$, which is not present in case A. That significant regeneration process is also observed in case III, in which the regenerated flow is more strengthened and disturbed because the initial flow Reynolds number and the velocity gradient in case III are larger and more significant. It is interesting to note that the maximum of the velocity fluctuations move to the hot wall and decrease in magnitude.

In fact, the fluctuations of velocities are related to the coherent behaviour of the near-wall turbulent structures. As discussed in Zonta, Marchioli & Soldati (2012*b*), the streak characteristics were altered due to the variation in viscosity. Patel *et al.* (2015)
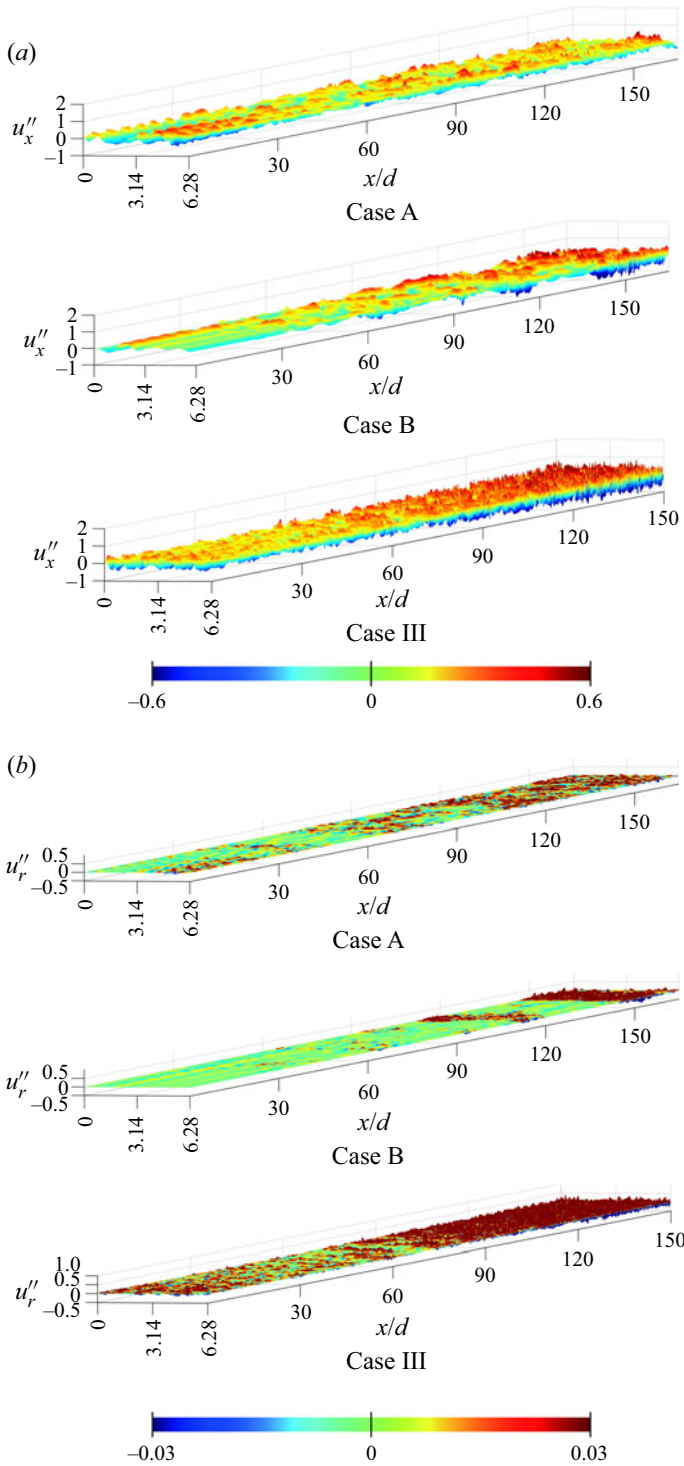
Figure 17. Instantaneous distributions of the (*a*) streamwise momentum and (*b*) wall-normal fluctuating velocities for cases A, B and III along spanwise coordinates at the near-wall region ($y^+ = 19$).
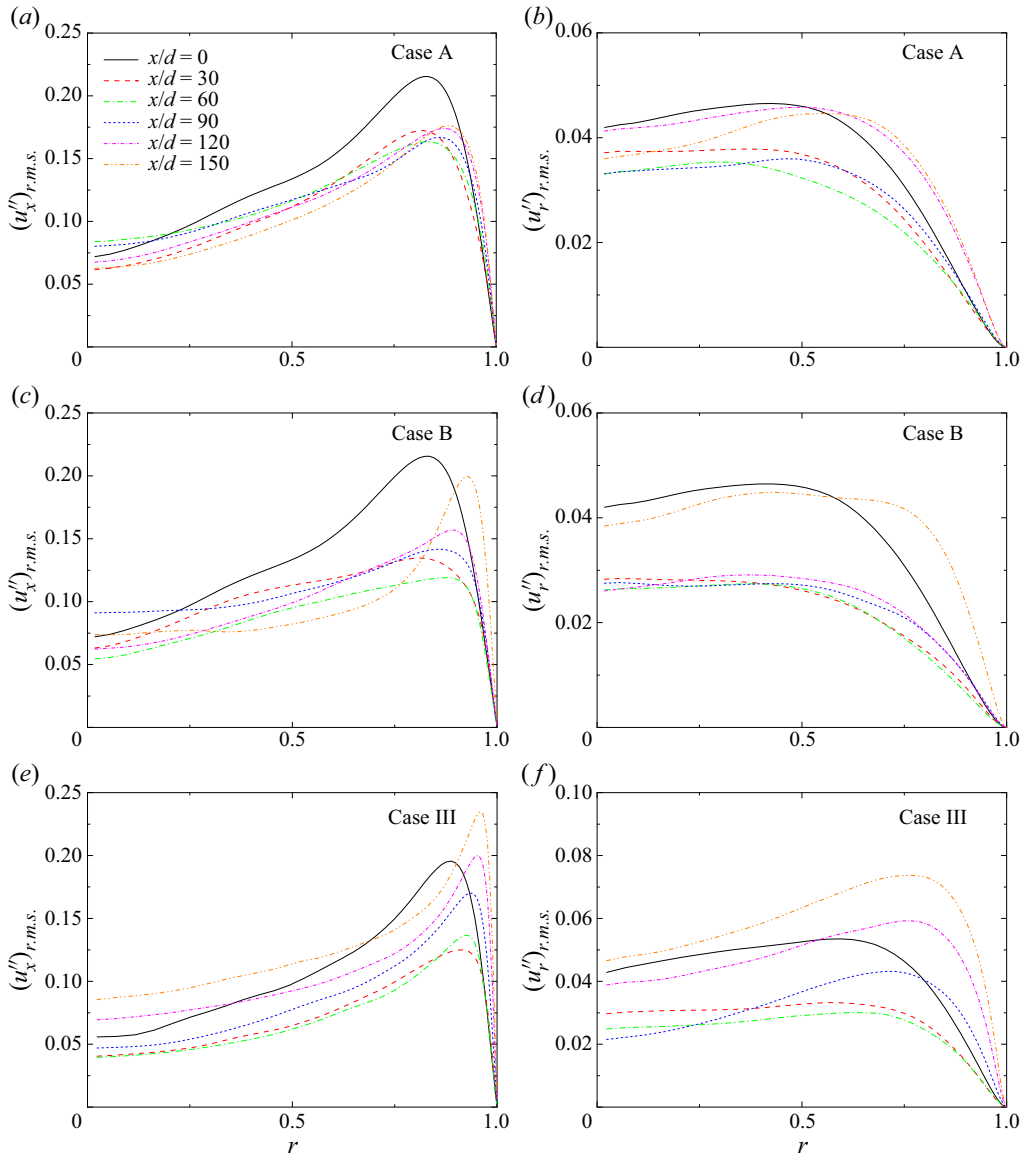
Figure 18. Root-mean-square profiles of streamwise (*a*) and wall-normal (*b*) velocity fluctuations for cases A, B and III at different axial locations.

stated that the stability of streaks was significantly affected by mean density and viscosity stratification. Combined with the findings of the authors in a previous study (Cao *et al.* 2021), the flow acceleration induced a stretch-to-disrupt mechanism of coherent turbulent structures and thus contributed to changes in the turbulent shear stress as well as the self-regeneration of near-wall turbulence. As a consequence, the variable properties and flow acceleration influenced the mean and instantaneous velocity fields. In fact, the fluctuating property itself dampenes the burst of streaks, although flow acceleration enhances the process in low-viscosity regions. The turbulence statistics and the near-wall turbulence structures are further discussed in the following section.
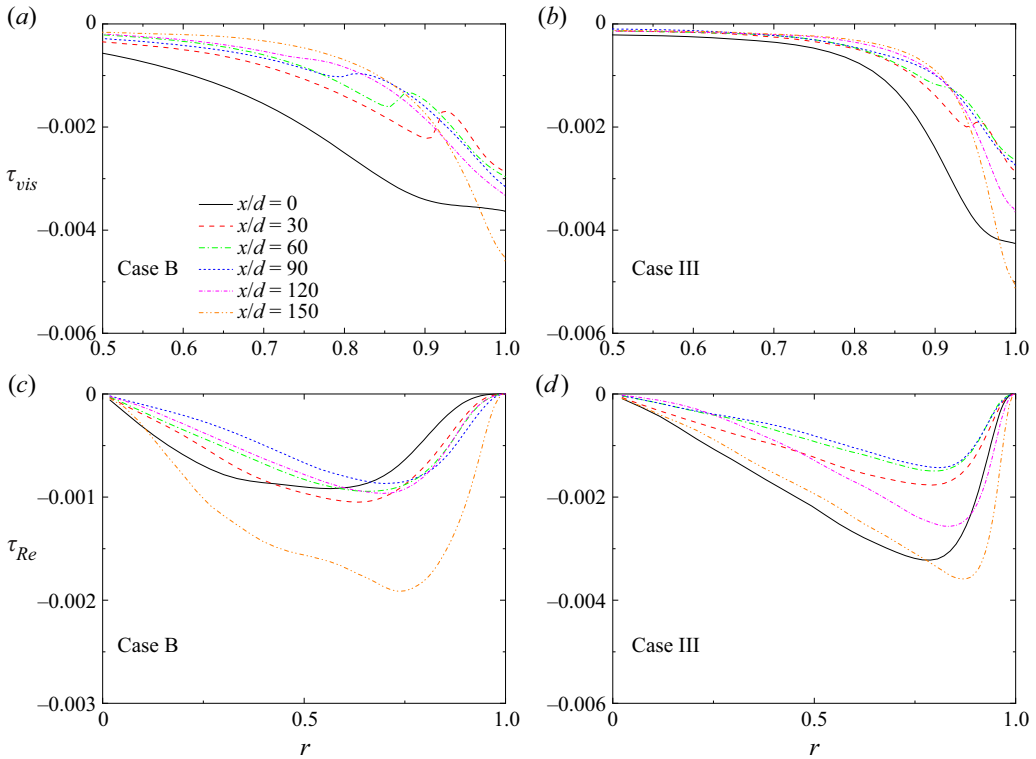
972 A13-28

Figure 19. Viscous stress and Reynolds shear stress in cases B and III.

3.4. *Turbulence statistics*

Due to a dramatic variation in density with temperature and pressure, the profiles of streamwise velocity changed with both magnitude and gradient at different axial locations, resulting in the development of profiles of shear stresses. The total shear stress in the (x, r) section consistes of the viscous stress $\tau_{vis} = Re_0^{-1} \bar{\mu} \partial \widetilde{u}_x / \partial r$, the fluctuating viscosity stress $\tau_{fluc} = Re_0^{-1} \overline{\mu' S'_{xr}}$, and the turbulent stress $\tau_{Re} = -\bar{\rho} \widetilde{u''_x u''_r}$, where S_{ij} represents the deviatoric stress tensor and μ' represents the dynamic viscosity fluctuation; notably, the scale of the second term is much less than the other two.

Thus, the fluctuating viscosity stress is negligible when analysing the profiles of the shear stresses. The developing profiles of both the viscous shear stresses and the Reynolds shear stresses are regarded as direct reflections of the velocity profiles. Figure 19(*a–d*) show the viscous stress as well as the turbulent shear stress for cases B and III. As the stresses directly scaled with the dynamic viscosity and density, the viscous stress and Reynolds shear stress shifted after the inlet in all cases. In the inlet region, the supercritical pressure fluids near the wall are quickly heated beyond the pseudocritical temperature, and consequently, the dynamic viscosity and density decrease abruptly in the near-wall region. Therefore, the changes in the shear stress profiles are attributed to the fluctuations of both dynamic viscosity and density. Since the Reynolds shear stress is an integral part of the generation of the near-wall turbulence, it is necessary to analyse the development of the profiles of Reynolds shear stress.

As the fluid temperature increases, the magnitude of density decreases, and the streamwise velocity profiles become flat due to acceleration (see figure 16). The turbulent

972 A13-29

shear stress declines significantly at $x/d = 0$–120, which means that less high-momentum fluid is transported from the bulk towards the wall, resulting in a smaller mean strain rate magnitude and thus a smaller wall shear stress. Although the mean strain rate magnitude at the wall increases slightly due to the flow acceleration, the significant decrease in dynamic viscosity at $x/d = 0$–20 contributes to a significant decrease in wall shear stress at the very beginning. After $x/d = 120$, the fluctuations of thermophysical properties at the near-wall region become small, and the magnitudes of dynamic viscosity remain a low level, but as the flow acceleration proceeds, the mean strain rate, especially in the buffer layer, recovered to some exceedance. Thus, the momentum exchange in the wall-normal direction is strong, and the Reynolds shear stress recovers to a high level. More high-speed momentum in the central region is transported to the wall; therefore, the mean strain rate magnitude at the wall recovered and the wall shear stress consequently increased. These results show that the mean profiles of both the dynamic viscosity and the density have an important influence on the viscous stress and Reynolds shear stress distribution. Compared with case III, which considers only thermal acceleration, case B, which is influenced by both pressure drop acceleration and thermal acceleration, shows a more severe decrease in Reynolds shear stress. In fact, the flow acceleration due to the pressure drop aggravates the deterioration of flow heat transfer, such as changes in total shear stress, production of turbulent kinetic energy and changes to turbulent structures. This is further discussed in subsequent sections.

The Reynolds shear stress is appreciably affected by thermophysical property variations and velocity profile stratification due to flow acceleration. Moreover, the magnitude of the turbulent kinetic energy is determined by the Reynolds shear stress and mean velocity profiles. Figure 20 shows the turbulence production and turbulent kinetic energy for case B. In addition to the increase in bulk velocity along the axial direction due to the decrease in a cross-sectional-average density, the bulk velocity also increases strongly due to a large pressure gradient. The developing profile of the streamwise velocity influence the Reynolds shear stress indirectly through the production $-\overline{\rho u_x'' u_r''} \partial \widetilde{u}_x / \partial x_r$, which is also the dominant term for turbulent production P_k. Strong reductions in both $\overline{\rho u_x'' u_r''}$ and P_k are observed during $30 < x/d < 120$. Correspondingly, turbulent kinetic energy k reaches the minimum which means strong suppression of turbulence. This is where the flow is fully laminar and a local wall temperature peak is observed nearby. After that, the maximum axial gradient of density moves to the core region, while the acceleration slows at the near wall region and the mean strain rate at that region recovers. This results in a recovered Reynolds shear stress in the core and the production of turbulence. Notably, the peaks of the production of turbulence and turbulence kinetic energy move towards the wall as the flow accelerates. The initial turbulence intensities are modulated under the flow acceleration, and the behaviour is explained as a response of the pre-existing turbulence to the property variations and flow acceleration. In fact, the transient flow progress turns out to be the redistribution of the mean velocity and fluctuation fields in the turbulent boundary layer by the various thermophysical properties and pressure.

The changes in turbulence intensities are closely associated with the turbulent convective heat transfer characteristics. The stronger the turbulent mixing is, the greater the convective heat transfer capacity. When the turbulent kinetic energy reaches the minimum, the turbulence is significantly attenuated, and the convective heat transfer coefficient decreases to a large degree. Therefore, for the constant wall heat flux, the steep peak of the wall temperature appears near $x/d = 80$ (figure 6a) where local heat transfer deterioration occurs, and then the wall temperature drops dramatically as the turbulence
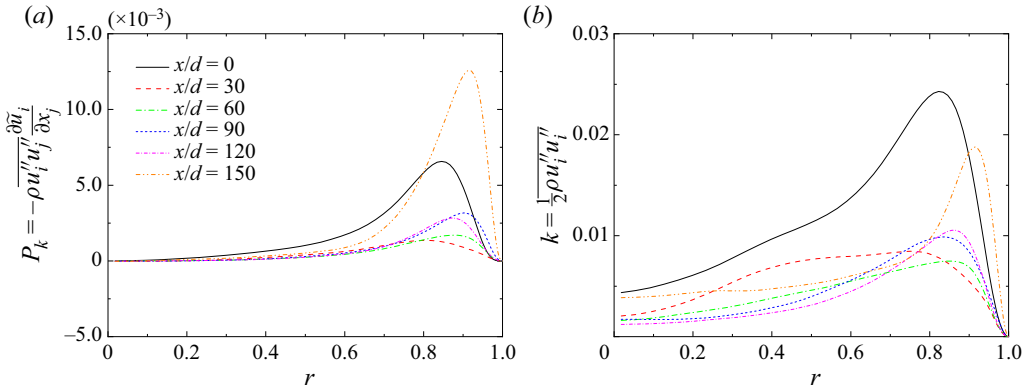
Figure 20. Distributions of turbulence production and turbulent kinetic energy for case B.

kinetic energy regenerates. Figures 19(*c*) and 20(*a*) show that the turbulence production at $x/d = 150$ is enhanced by approximately two times compared with the initial value, but the recovery of the Reynolds shear stress at $x/d = 150$ is not as obvious. This suggests that the large mean strain rate makes an important contribution to turbulence regeneration. The mean strain rate $\partial \overline{u}_x / \partial r$ increases in the highly accelerated flow in the low-viscosity region near the wall but decreases upstream due to the high dynamic viscosity.

The turbulent structures are also of great importance to the production of turbulent kinetic energy since the formation of streamwise vortices and near-wall streaks as well as their instabilities are an integral to the self-regeneration process of near-wall turbulence. According to figure 20, the heat transfer deterioration occurs while the turbulent kinetic energy reaches a lower value but still remains significant in magnitude; however, the heat transfer capacity of turbulent flow shows the characteristics of laminar flow. In this paper, the term quasilaminar region refers to a region where no new vortical structures are generated. This suggests that in the quasilaminar region, the decaying turbulence fluctuations might still be significant, but the self-regeneration of turbulence structures is disrupted, leading to attenuated turbulent mixing behaviour and consequently leading to the turbulence heat transfer deterioration. In the following discussion, we further investigate the effects on the turbulent structures in terms of the scale effect, thermophysical property variation and flow acceleration.

3.5. *Turbulent structures*

The fluctuations of wall turbulence are assumed to be generated by near-wall coherent structures. In the turbulent boundary layer, the maximum fluctuation velocity intensity occurs at approximately $y^+ = 15$, while the maximum Reynolds stress occurs at approximately $y^+ = 30$, where the strip undergoes vibration and rupture. Thus, the bursting behaviour of wall turbulence is the mechanism that generates turbulent pulsations and Reynolds stresses. Therefore, in this section, we study the behaviour of turbulent structures to reveal the turbulence regeneration mechanism and identify the representative structures with a view to modifying the turbulence to achieve engineering goals such as enhancement of heat transfer and reduction of pressure drop.

The first important mechanism in the common characteristic coherent pattern is the streaks that occurs in the region $0 < y^+ < 10$. The effects of flow acceleration and variable properties on the steaks are investigated. The flow visualization in figure 21 reveals the
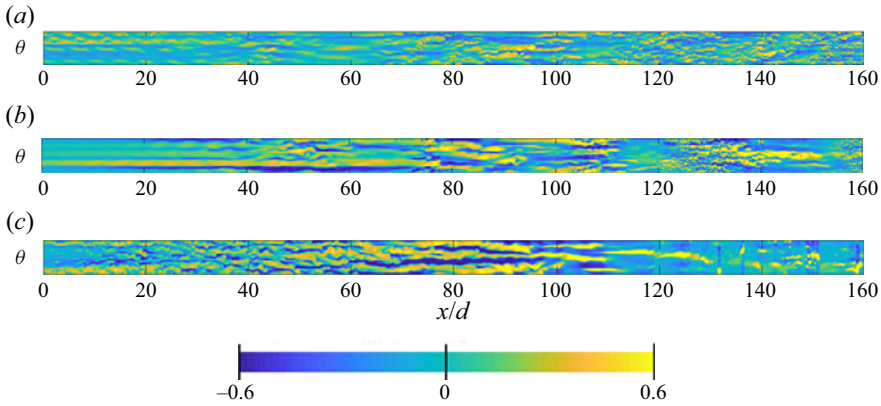
Figure 21. Contour plots of the streaks $(\rho u_x)'$ for case A, case B and case C at the near-wall region ($y^+ = 8$).

streaks in the near-wall region ($y^+ = 8$). The figure clearly shows that the magnitude of $|(\rho u_x)'|$ remains significant along the acceleration process; however, the pattern of the streaks is obviously distorted in cases B and C, especially in the reverse-transitional and quasilaminar regions. In case B, the stratification of high-speed and low-speed streaks is evident at $x/d = 80$, and the streamwise length of the streaks is obviously stretched (see figure 21b). Downstream at $x/d = 120$ in case B, disorganized streaks appear again as the turbulence gradually regenerated. The change in the streaks morphology is more obvious in case C. Since the streaks are largely related to the turbulent shear stress, the above observations are consistent with our earlier observations in §3.4. Low-speed streaks are believed to be traces of streamwise vortices; therefore, the change in the streak structure from disorganized to rarefied visually indicates the stages of turbulence flow (§3.1). For instance, in case B, the turbulent heat transfer deterioration occurs at $x/d = 30$–120, showing a steep temperature peak, and recovers downstream as a result of turbulence regeneration.

Notably, in the bulk accelerating flow, we found a different change in the structures of the steaks. However, in the most deteriorated stages, the streak structures do not decrease uniformly in the near-wall region as found by Peeters *et al.* (2016). Under the effects of thermophysical property fluctuations, they appear intermittently as more significant large-scale structures. Therefore, we extracted the velocity profiles from individual streak realizations to quantitatively investigate streak motions. As illustrated in figure 22(a), the bold contour indicates the typical cross-section of the lifted streaks; the streamwise velocity profiles at different regions are discussed below. To evaluate the instability of streaks, we analysed the wavenumbers of the spanwise disturbances in accordance with Floquet theory,

$$\begin{pmatrix} u' \\ v' \\ w' \\ p' \end{pmatrix} (x, y, z, t) = \text{Real} \left[\begin{pmatrix} \tilde{u} \\ \tilde{v} \\ \tilde{w} \\ \tilde{p} \end{pmatrix} (y, z) \exp(\mathrm{i}(\alpha x + \beta z)) \mathrm{e}^{\sigma t} \right], \quad (3.11)$$

where α and β are the streamwise and spanwise streak wavenumbers, respectively, with eigenvalues $\sigma = \sigma_r + \mathrm{i}\sigma_i$. The complex eigenfunctions are periodic in the spanwise direction. As shown in figure 22(b), at the beginning of flow acceleration, high-frequency and large-magnitude periodic low-speed streaks are lifted from the wall. In this region,
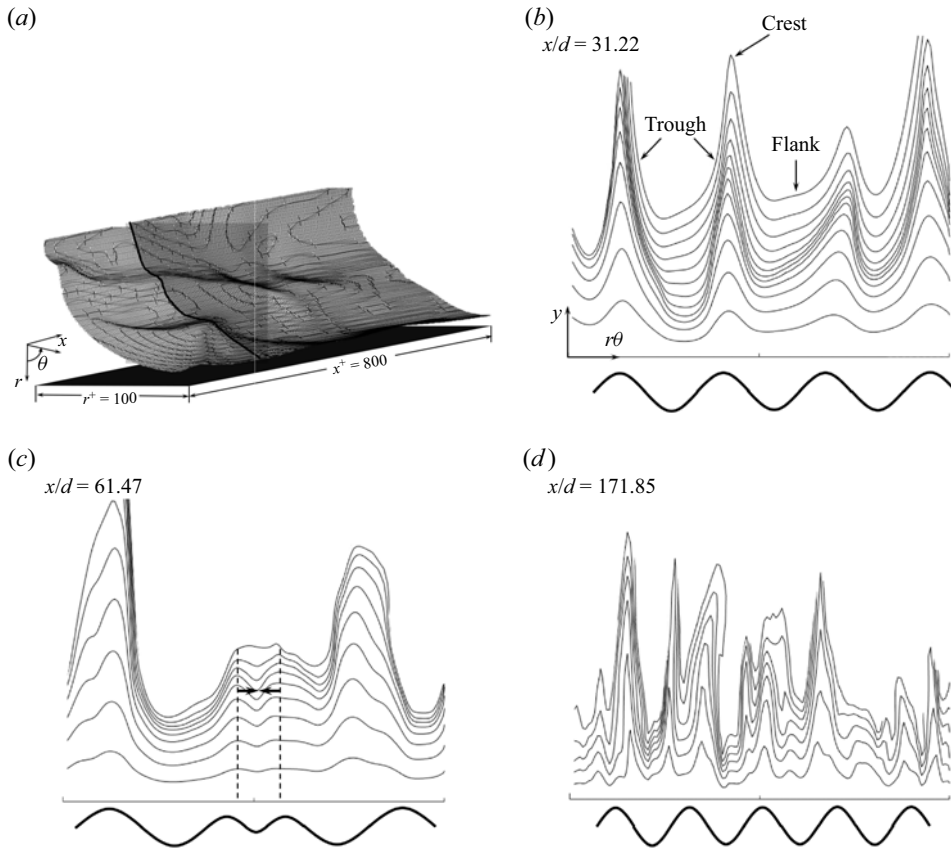
972 A13-32

Figure 22. Low-speed streak realization in the near-wall region: (*a*) 0.55 U_0 isosurface; (*b*–*d*) contour line of streamwise velocity U_x at cross-stream section. The dashed lines in (*c*) denote the crests of the middle two streaks.

the wavenumber β of the streaks and the strength of the lifted streaks are basically constant. However, as the flow acceleration proceeds, the flow velocity field distribution is distorted, resulting in decreasing mean strain rate and therefore decreasing Reynolds shear stress near the wall (see figure 19). The smaller mean strain rate means fewer low-speed fluids are transformed from the wall to the centre of the tube. Therefore, with this negative normal momentum exchange, the magnitude of the streaks is expected to decrease substantially, as the smaller wave crests show in figure 22(*c*). However, as the flow acceleration accompanies more significant positive streamwise velocity fluctuations in the flow centre, the high-speed fluid is transformed from the centre to the wall, contributing to new disturbances to the flow with a larger spanwise wavenumber β_0 superimposed on existing perturbations. At $x/d = 171.85$, the perturbation order is re-established due to the recovery of the average deformation rate, which is consistent with the regeneration of the strips shown in the previous visualization.

According to previous studies (Bae *et al.* 2005; Nemati *et al.* 2015), it is necessary to define the momentum vorticity as $\boldsymbol{\omega} = \nabla \times (\rho\boldsymbol{u})$ by considering the density variation for fluids under supercritical pressure. Figure 23 provides the distributions of instantaneous streamwise momentum vortices $\omega_x = (1/r)(\partial(r\rho u_\theta)/\partial r - \partial(\rho u_r)/\partial\theta)$. To explain the perturbation vorticity generation mechanism, we derived the vorticity perturbation
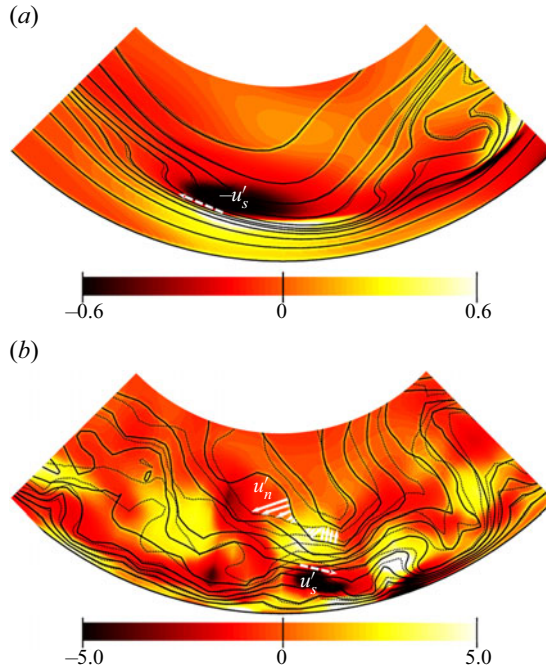
(*a*)

−0.6　　　0　　　0.6

(*b*)

−5.0　　　0　　　5.0

Figure 23. Contours of streamwise momentum vorticity ω_x in case B: (*a*) $x/d = 80$; (*b*) $x/d = 170$. Solid lines denote the contours of streamwise velocity at moment $= n$ s. Dashed lines denote the contours of streamwise velocity at moment $= n + 10^{-6}$ s.

equations in the streak-vortex-line coordinate system (x, n, s), where the s and n directions denote the tangent and normal directions to the base-flow vortex lines, respectively. By performing the coordinate system transformation, we significantly simplified the evolution equations for perturbation vorticity (Schoppa & Hussain 2002) to the following form:

$$
\left.
\begin{aligned}
\frac{\partial \omega_x'}{\partial t} + U \frac{\partial \omega_x'}{\partial x} &= h_s \Omega \frac{\partial u_x'}{\partial s} + h_n \omega_n' \frac{\mathrm{d}U}{\mathrm{d}n} = \Omega \frac{\partial u_s'}{\partial x}, \\
\frac{\partial \omega_n'}{\partial t} + U \frac{\partial \omega_n'}{\partial x} + h_s h_n \Omega u_n' \frac{\partial (1/h_n)}{\partial s} &= h_s \Omega \frac{\partial u_n'}{\partial s}, \\
\frac{\partial \omega_s'}{\partial t} + U \frac{\partial \omega_s'}{\partial x} + h_s u_s' \frac{\partial \Omega}{\partial n} + h_n u_n' \frac{\mathrm{d}\Omega}{\mathrm{d}n} &= h_s \Omega \frac{\partial u_s'}{\partial s} + h_s h_n \Omega u_n' \frac{\partial (1/h_s)}{\partial n},
\end{aligned}
\right\}
\tag{3.12}
$$

where h_s, h_n, Ω are determined from

$$
h_s^2 = \left(\frac{\partial n}{\partial r}\right)^2 + \left(\frac{1}{r}\frac{\partial n}{\partial \theta}\right)^2, \quad h_n^2 = \left(\frac{\partial s}{\partial r}\right)^2 + \left(\frac{1}{r}\frac{\partial s}{\partial \theta}\right)^2, \quad \Omega = -h_n \, \mathrm{d}U/\mathrm{d}n. \quad (3.13a\text{--}c)
$$

To understand the right-hand side of ω_x', we concluded that the generation of perturbation streamwise vorticity consisted of two tilting terms. By introducing the base-flow vorticity Ω we further simplified the original tilting terms to one term $\Omega \partial u_s'/\partial x$. The sole generation term clearly explains the mechanism of ω_x' generation by the mean shear motions, illustrating the vortex generation in both the quasilaminar and retransition regions due to significant flow acceleration. In the quasilaminar region, there is apparent

972 A13-34

local shear as the deformed near-wall streaks provide apparent high-speed and low-speed flow stratification. The vector of u'_s is represented in the crest top. The initial u'_s regions from the spanwise motion undergo shear deformation by the base flow shear $\mathrm{d}U/\mathrm{d}n$, resulting in the advection of $+u'_s$ to $-u'_s$. Consequently, a spanwise shear layer of u'_s is generated, which is the form of streamwise vorticity perturbation $+\omega'_x$ in the region where $\partial u'_s/\partial x$ is negative and symmetrically $-\omega'_x$ is generated in the region where $\partial u'_s/\partial x$ is positive. Notably, u'_n is extremely small in this region, resulting in the restrained generation of ω'_n, which is dominated by $h_s\Omega\partial u'_n/\partial s$. Subsequently, the $+\omega'_x$ generated is further advected under the bottom of $-\omega'_x$, resulting in z-elongated sheets of ω'_x, as shown in the figure. Downstream at $x/d = 170$, in addition to the ω'_x generation due to mean shear, the magnitude of $\partial u'_n/\partial s$ is large compared with that at $x/d = 80$, resulting in the recovered generation of $h_s\Omega\partial u'_n/\partial s$ and hence of ω'_n and ω'_s.

The vorticity distribution also corresponds to the flow region due to the inherent disturbances to the vorticity structures of the corresponding streaks. During the region where the streak disturbances are normal in regions I and IV (see figure 10), and the spanwise wavenumber is large and successive, vorticity perturbations are also generated in the normal mode. However, the perturbations are susceptible to accelerated flow velocity profiles. As the velocity profiles are distorted, the original streak perturbations decay fast, changing the dominant perturbation to high-speed bulk flow transformed to the wall. The new perturbation mode eventually evolves into the generation of streamwise vorticity due to tangential shear and the attenuation of the other vortices. This kind of unstable mode is temporary in the heated turbulent flow at supercritical pressure since the highly accelerated flow will retransition to full turbulence in the downstream low-viscosity region. In the retransition region, in contrast to the quasilaminar region, the generation of turbulent structures recover to a large extent, even beyond the initial turbulence.

We further investigated the integrated vortical structures by the Q criterion to visually illustrate the dynamics of the development of turbulence. The Q criterion is defined as the second invariant of the velocity gradient $Q = 0.5(S_{ij}^2 - s_{ij}s_{ji} - W_{ij}W_{ij})$, where the strain rate tensor is $s_{ij} = 0.5(A_{ij} + A_{ji})$, the skew-symmetric rotation rate tensor is $W_{ij} = 0.5(A_{ij} - A_{ji})$, and the velocity gradient tensor is $A_{ij} = \nabla u$. Figure 24 shows the evolution of vortical structures for cases A–C at three different locations $x/d = 10, 80, 120$. As clearly shown, the vortical structures in the first column at left are intensive in the original turbulent region. The turbulence laminarization is revealed by the reduction in the strength of vorticity motions. For the quasilaminar regions, such as $x/d \approx 80$, the vorticity motions become so weak that the isosurfaces are sparse. More specifically, the coherent hairpin vortex with a large-scale is strongly inhibited to almost invisible due to the flow acceleration effects discussed before. Note that there remains some long finger/stick-like structures (also several spanwise prolate structures) corresponding to the generation mechanism of streamwise vorticity in this region. The high-shear heads of the hairpin vortex are partly destroyed, resulting in less coherent behaviour. Subsequently, in the retransition region, large-scale vortex sheets regenerated, evolving more eddies and therefore the coherent behaviours produces strong turbulent fluctuations.

3.6. *Additional effects*

3.6.1. *Scale effect*

Owing to the scale effect of the micron pipe, the dimensional viscous stress $\overline{\mu^*}\partial\widetilde{u_x^*}/\partial r^*$ in the viscous layer was much greater than that in the tubes with millimetre diameters.
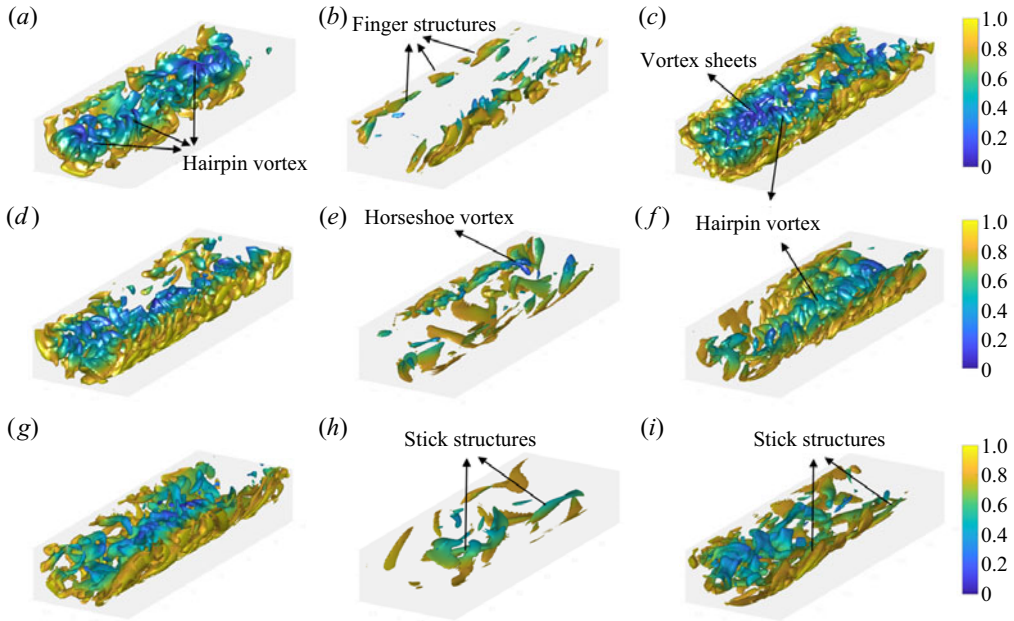
Figure 24. Temporal evolution of vortical structures for case A (*a–c*), case B (*d–f*) and case C (*g–i*) at times $x/d = 10$, 80, and 120 in (*a,d,g*), (*b,e,h*) and (*c,f,i*), respectively. The vortical structures are identified by isosurfaces of $Q = 0.001$ for all cases.

Figure 25 shows the effect of scale on the magnitude of the wall shear stress of turbulent flow at supercritical pressure in vertical tubes. As the figure shows, the wall shear stress in the micron tubes with diameter 0.0992 mm is approximately two orders of magnitude larger than that in tubes with diameters 1–3 mm, which contributes to a larger frictional pressure drop. The scale effect also has a significant influence on the generation of wall vortex structures for wall turbulence. The scale of the near-wall structure of wall turbulence is inversely proportional to the magnitude of the friction velocity. Cantwell (1981) obtained the characteristic parameters of the coherent structure of wall turbulence. For example, the average width of the bottom steaks of wall turbulence was $100\nu/u_\tau$, in which the friction velocity is $u_\tau = \sqrt{\tau_w/\rho}$.

The turbulent structure behaviour is a key component in the process of turbulence generation. The DNS results revealed that the turbulent coherent structures of accelerating turbulent flow in micron tubes are influenced to distort and even disappear in the quasilaminar region. The structures of the long and narrow low-speed stripes and the short and wide high-speed stripes structure are shown in § 3.5. It directly influences the turbulent mixing motion and convection heat transfer ability. In micron tubes, the average width of the bottom steaks is expected to be one order of magnitude smaller than that in large-scale tubes. Figures 26 and 27 show the details of the characteristic parameters of the turbulence coherent structures obtained from DNSs. Typical vortex structures are shown in contours in the micron tube in the initial turbulent region. Isosurfaces of streamwise vorticity ω_x and spanwise vorticity ω_r at levels $> +0.6\omega_i|_{max}$ and $< -0.6\omega_i|_{max}$ are shaded in red and blue, respectively. The threshold value of $0.6\omega_i|_{max}$ is chosen according to Schoppa & Hussain (2002), who provided a comprehensive understanding of the generation mechanism of near-wall vortices. Limited to the micron radial scale, the dimensional scale of the boundary layer is very small, leading to a thin but strong shear layer along with quadrant Reynolds stresses and especially large-scale turbulence structures at the near-wall region.
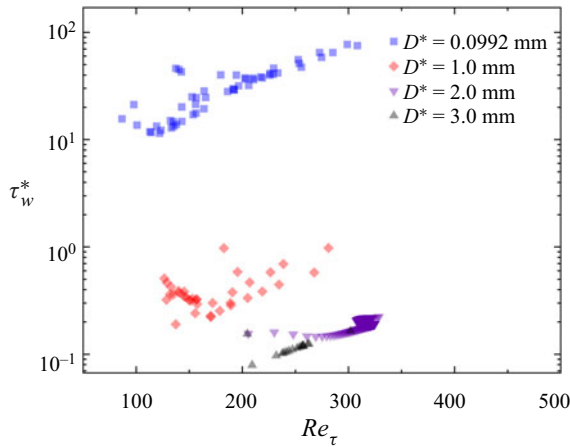
Figure 25. Wall shear stress of turbulent flow at supercritical pressure in vertical tubes with different diameters. Black and purple dots denote results in tubes with $D^* = 3.0$ and 2.0 mm, respectively, from DNSs by Bae *et al.* (2005). Red dots denote results in tubes with $D^* = 1.0$ mm, from Cao *et al.* (2021). Blue dots denote results from the present study, for tubes with $D^* = 0.0992$ mm.

As shown in figure 26(*a,b*), the streamwise vortices generated in the initial turbulence in the micron tube are visualized and the dimensional scale is calculated at different radial locations. Apparently, the vortex generation mechanism is inherently three-dimensional, as it is intensely stretched in the streamwise direction with a significant gradient $\omega_x \partial u/\partial x$, and tilting and convection terms are necessary. The micron-scale magnifies the effects of the wall with curvature. Due to the complexity of the vortex structure in the flow field, the vortex shape in the transient flow field obtained by visualization is not a regular circle and exists eccentricity. To quantitatively analyse the distribution of the vortex scale, the network lattice method is used in this study to approximately characterize the scale of the vortex. The number of normal detection lattices multiplied by the edge length is taken as the normal width of the vortex structure. The schematic diagram for calculating the mean diameter of the vortex is given in the subfigure, and the average width $D^+ = Du_\tau/\nu$ results are shown in figure 26(*b*). The average width of the prograde vortex is shown in the solid label and line, and in the hollow label and line of the retrograde vortex. For both the prograde vortex and retrograde vortex, the width increases and then decreases along the non-dimensional wall distance and shows a local maximum at $y^+ \approx 30$. Notably, the width is defined as the wall-normal length of the vortex, and the width of the streamwise vortices in the centre region is approximately $\sim 70 \, \nu/u_\tau$ wide. and it is clear that the streamwise vortices are narrow than the typical wall-normal length of vortex $100\nu/u_\tau$ in the centre region for wall turbulence in normal-scale channels.

The same method is used to calculate the average wall-normal height H^+ for spanwise vorticity, as shown in figure 26(*c,d*). The width of the near-wall spanwise vortices at $y^+ = 30$ is approximately 15–$20\nu/u_\tau$, which is coincident with a previous study (Cantwell 1981). However, the average height in the centre region decreases to some extent, which means that the near-wall spanwise convection to the centre region is limited. The streak width at $y^+ = 5$ is studied and compared in regions I and II using the autocorrelation method on the streamwise velocity fluctuations. In the initial turbulence region, the width of the streak is $100\nu/u_\tau$, which does not differ much from that in a regular diameter channel. The high-speed streak width in the quasilaminar region is approximately 150–$160\nu/u_\tau$, bigger
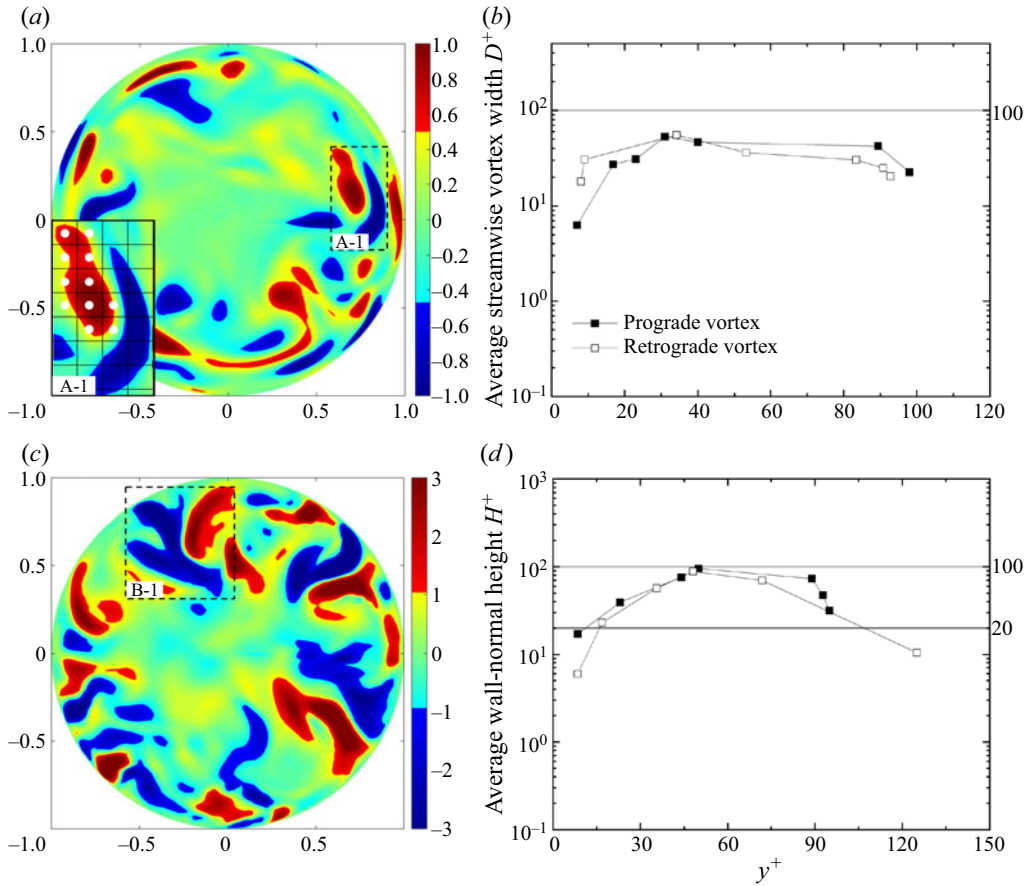
Figure 26. Characteristic parameters of the turbulence vortices were obtained from direct numerical simulations. (*a,b*) Schematic diagram and scale of streamwise vortex, respectively. (*c,d*) Schematic diagram and scale of wall-normal vortex, respectively. Here: (*a*) ω_x; (*b*) D^+ of ω_x; (*c*) ω_r; (*d*) H^+ of ω_r.

than that of the initial turbulence flow. This is attributed to the new perturbance mode induced by the distorted velocity profiles as discussed in § 3.5.

The scale effect on the coherent structures in the figures further influences the underlying mechanism of the burst events. The burst events occurring in the near-wall region are the dominant processes producing turbulent fluctuations and Reynolds stress. As seen in the quadrant analysis of Reynolds stress and the comparison of burst event strengths, the velocity fluctuations in the radial direction are very different from those in conventional tubes, which is where the effect of wall curvature takes effect. More specifically, observations of $-\overline{u'v'}$ Reynolds stress events of quadrant Q4 (sweep, $u' > 0$; $v' < 0$) make more contributions to Reynolds stress than the quadrant Q2 (eject, $u' < 0$; $v' > 0$). The Reynolds stress events of quadrant Q4 contributed 60 % of the magnitude of the Reynolds stress. That is opposite in the normal-scale tubes, where at $y^+ = 30$ the Q2 events are expected to contribute 70 % of the magnitude of the Reynolds stress while the Q4 events are expected to contribute approximately 30 %. The results indicate the prominent role of the specific turbulence generation mechanism in accelerating turbulence in micron tubes and suggest promising robust control of drag and heat transfer considering the same conditions.
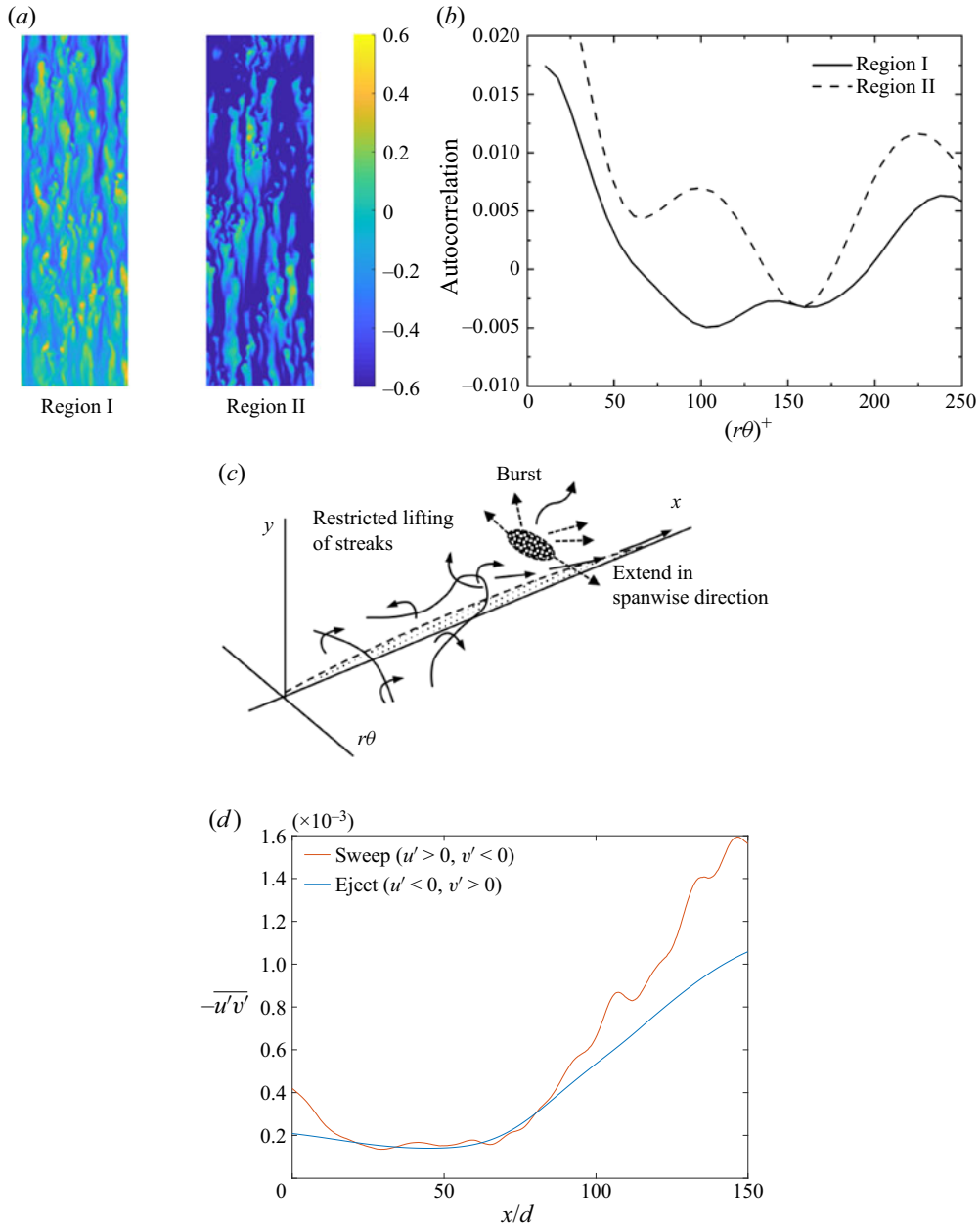
972 A13-38

Figure 27. Characteristic parameters of the near-wall streaks were obtained from direct numerical simulations. (*a,b*) The scale of typical near-wall streaks at $y^+ = 5$ in micron tube based on autocorrelation analysis of the velocity of flow direction pulsation. (*c*) Qualitative description of burst events with scale effect. (*d*) Distribution of $-\overline{u'v'}$ at $y^+ = 30$.

3.6.2. *Mean pressure gradients*

According to the prior analysis, the effects of mean pressure gradients on turbulent dynamics could be large in micron tubes. Due to the negative density gradient along the streamwise direction ($\mathrm{d}\rho/\mathrm{d}x < 0$) and frictional pressure drop, the negative pressure gradient ($\mathrm{d}P^{*(0)}/\mathrm{d}x < 0$) is large in the micron tubes. In engineering applications, the

negative pressure gradient is favourable more often than not. For example, on the forward part of an airfoil, the negative pressure gradient contributes to the streamwise flow. The negative streamwise pressure gradients and density gradient together cause the mean streamwise velocity profile to steepen. In the constant low-viscosity region, the skin friction coefficient C_f increases (see figure 9c), resulting in increasing pressure gradients. A sufficient negative pressure gradient can cause the boundary layer to relaminarize (Narasimha & Sreenivasan 1973). As a consequence, for the cases considered in this study, turbulence relaminarization is attributed to the pressure-driven and property variation-driven contributions. For supercritical pressure cases in our simulation, the first part is considered in all cases, and the second part is considered differently, as the pressure influence on the properties is obvious in low inlet pressure cases but ignored in high inlet pressure cases. This influence is illustrated quantitatively by the isothermal compression coefficient in different cases. The effects of the flow acceleration are more significant at relatively lower pressures close to pseudocritical and lower inlet Reynolds numbers. For the second kind of case, flow acceleration is partly driven by the mean pressure drop. According to the previous discussion, the pressure drop driven flow acceleration has a stabilizing effect on the perturbation of the turbulent flow, which suppresses the turbulent mixing heat transfer process in the boundary layer; thus the heat transfer is reduced. This understanding will help in the design of better heat transfer models by considering the mean pressure gradient, such as Nusselt number relationships and turbulence models.

4. Conclusions

The characteristics of turbulent heat transfer to supercritical pressure CO_2 flowing in heated micron tubes were investigated with DNS in this study. Due to the very large temperature and pressure gradients along the flow direction, significant flow acceleration and variable thermophysical properties were induced in micron tubes, which influenced the corresponding turbulent dynamics as well as the heat transfer performance. Comparing the cases with the pressure drop and constant pressure, the worst deteriorated point of flow heat transfer moved downstream, and the peak wall temperature was higher. Considering the change of pressure, the deviation on temperature distribution because of physical properties was more than 10 K. The physical mechanism of the heat transfer deterioration phenomena under the effects of flow acceleration and variable thermophysical properties was investigated. Unlike the well-known buoyancy-caused heat transfer deterioration, the maximum deterioration of heat transfer was found to occur in a region of reduced turbulence regardless of the flow direction. Farther downstream where the highly accelerated turbulence generation mechanism was restored in the low-viscosity region, turbulent heat transfer was gradually recovered.

To reveal the underlying association between turbulence intensities and heat transfer characteristics, flow development under continuous flow acceleration was divided into four regions. The shear stress at the near-wall region had a the prominent influence on production of turbulence. The mean strain rate $\partial \overline{u_x}/\partial r$ increased in the highly accelerated flow in the low-viscosity region near the wall but decreased upstream due to the high dynamic viscosity. And the developing profile of the streamwise velocity influenced the Reynolds shear stress indirectly through the production $-\overline{\rho u_x'' u_r''} \partial \widetilde{u_x}/\partial x_r$, which led to decreased production of turbulent kinetic energy and structures in regions II and III. In region IV, the recovered generations of mean shear and perturbation vorticity contributed to retransition in the high Reynolds flow. Flow acceleration accompanied more significant positive streamwise velocity fluctuations. Since the formation of streamwise vortices and near-wall streaks as well as their instabilities were an integral part of the self-regenerating

process of near-wall turbulence, the generation of turbulent structures generation scenario was further studied to explain the attenuated turbulence.

Notably, in the bulk accelerating flow, we observed a different change in the structures of the steaks. However, in the most deteriorated stages, the streak structures did not decrease uniformly in the near-wall region, and instead appeared intermittently with more significant large-scale structure. The high-speed streak width in the quasilaminar region was approximately 150–$160 \nu/u_\tau$. The high-speed fluid was transformed from the centre to the wall, contributing to a new disturbance scenario of the flow with a larger spanwise wavenumber superimposed on existing perturbations. In the region where the streak disturbances were normal in the original turbulence and the spanwise wavenumber was large and successive, the generation of vorticity perturbations also occurred in the normal mode. As the velocity profiles were distorted, the original streak perturbations decayed fast, forming a new perturbation mode that enabled the generation of streamwise vorticity due to tangential shear and the attenuation of other vortices. The initial u'_s generated from the spanwise motion underwent shear deformation by the base flow shear $\mathrm{d}U/\mathrm{d}n$ maintained the generation of perturbation streamwise vorticity in the quasilaminar region. More specifically, the large-scale coherent hairpin vortex was strongly inhibited to be almost invisible due to the flow acceleration effects. There were some long finger/stick-like structures (also several spanwise prolate structures) corresponding to the mechanism of generation of streamwise vorticity in the quasilaminar region.

Further investigation of additional effects in micron tubes was conducted to support the possibilities of inhibiting the deterioration of heat transfer. The effects of mean pressure gradients on turbulence dynamics can be large in micron tubes. A sufficient negative pressure gradient caused the boundary layer to relaminarize. The scale effect inhibited the vortex advection and lifted motion to the centre region, resulting in a vortex compressed in the wall-normal direction. As a consequence, the related burst events showed a different pattern compared with turbulence in normal-scale tubes. We revealed that the Reynolds stress events of quadrant Q4 contributed 60 % of the Reynolds stress, greater than those of quadrant Q2 to the Reynolds stress due to scale effect.

Declaration of interests. The authors report no conflict of interest.

Author ORCIDs.

- Yuli Cao https://orcid.org/0000-0002-2518-0744;
- Ruina Xu https://orcid.org/0000-0001-8561-560X;
- S. He https://orcid.org/0000-0003-0326-2447;
- Peixue Jiang https://orcid.org/0000-0002-9777-8075.

REFERENCES

ABE, H. 2001 Direct numerical simulation of a fully developed turbulent channel flow with respect to the Reynolds number dependence. *Trans. ASME J. Fluids Engng* **123**, 382–393.

AHMAD, T., HASSAN, I. & MEGAHED, A. 2015 Experimental investigation of turbulent heat transfer in the entrance region of microchannels. *J. Thermophys. Heat Transfer* **24**, 388–399.

AZIH, C. & YARAS, M.I. 2018 Effects of spatial gradients in thermophysical properties on the topology of turbulence in heated channel flow of supercritical fluids. *Phys. Fluids* **30**, 015108.

BAE, J.H., YOO, J.Y. & CHOI, H. 2005 Direct numerical simulation of turbulent supercritical flows with heat transfer. *Phys. Fluids* **17**, 105104.

BAE, J.H., YOO, J.Y. & MCELIGOT, D.M. 2008 Direct numerical simulation of heated CO_2 flows at supercritical pressure in a vertical annulus at $Re = 8900$. *Phys. Fluids* **20**, 34–43.

CANTWELL, B.J. 1981 Organized motion in turbulent flow. *Annu. Rev. Fluid Mech.* **13**, 457–515.

CAO, Y.L., XU, R.N., YAN, J.J., HE, S.S. & JIANG, P.X. 2021 Direct numerical simulation of convective heat transfer of supercritical pressure CO_2 in a vertical tube with buoyancy and thermal acceleration effects. *J. Fluid Mech.* **927**, A29.

EGGELS, J.G.M., UNGER, F., WEISS, M.H., WESTERWEEL, J., ADRIAN, R.J., FRIEDRICH, R. & NIEUWSTADT, F.T.M. 1994 Fully developed turbulent pipe flow: a comparison between direct numerical simulation and experiment. *J. Fluid Mech.* **268**, 175–209.

EHSAN, M., AWAIS, M., LEE, S., SALEHIN, S., GUAN, Z.Q. & GURGENCI, H. 2023 Potential prospects of supercritical CO2 power cycles for commercialisation: applicability, research status, and advancement. *Renew. Sust. Energy Rev.* **172**, 113044.

HALL, W.B. 1971 Heat transfer near the critical point. *Adv. Heat Transfer* **7**, 1–86.

HALL, W.B. & JACKSON, J.D. 1969 Laminarization of a turbulent pipe flow by buoyancy forces. In *11th ASME-AIChE National Heat Transfer Conference*. ASME. 69-HT-55.

HE, J., TIAN, R., JIANG, P.X. & HE, S. 2021 Turbulence in a heated pipe at supercritical pressure. *J. Fluid Mech.* **920**, A45.

HE, S., KIM, W.S. & BAE, J.H. 2008 Assessment of performance of turbulence models in predicting supercritical pressure heat transfer in a vertical tube. *Intl J. Heat Mass Transfer* **51**, 4659–4675.

HE, S., KIM, W.S., JIANG, P.X. & JACKSON, J.D. 2004 Simulation of mixed convection heat transfer to carbon dioxide at supercritical pressure. *J. Mech. Engng Sci.* **218**, 1291–1296.

HE, S. & SEDDIGHI, M. 2013 Turbulence in transient channel flow. *J. Fluid Mech.* **715**, 60–102.

HEGAB, H.E., BAN, A. & AMEEL, T. 2002 Friction and convection studies of R-134A in microchannels within the transition and turbulent flow regimes. *Expl Heat Transfer* **15**, 245–259.

JACKSON, J.D. 2001 Some striking features of heat transfer with fluids at pressures and temperatures near the critical point. In *Proceedings of the International Conference on Energy Conversion and Application* vol. 1, pp. 50–61.

JACKSON, J.D. 2002 Consideration of the heat transfer properties of supercritical pressure water in connection with the cooling of advanced nuclear reactors. In *Proceedings of the 13th Pacific Basin Nuclear Conference*.

JACKSON, J.D. & HALL, W.B. 1979 Influences of buoyancy on heat transfer to fluids flowing in vertical tubes under turbulent conditions. In *Turbulent Forced Convection in Channels and Bundles*, vol. 2, pp. 613–640. Hemisphere.

JAJJA, S.A., ZADA, K.R. & FRONK, B.M. 2019 Experimental investigation of supercritical carbon dioxide in horizontal microchannels with non-uniform heat flux boundary conditions. *Intl J. Heat Mass Transfer* **130**, 304–319.

JIANG, P.X., LIU, B., ZHAO, C.R. & LUO, F. 2013 Convection heat transfer of supercritical pressure carbon dioxide in a vertical micro tube from transition to turbulent flow regime. *Intl J. Heat Mass Transfer* **56**, 741–749.

JIANG, P.X., WANG, Z.C. & XU, R.N. 2018 A modified buoyancy effect correction method on turbulent convection heat transfer of supercritical pressure fluid based on RANS model. *Intl J. Heat Mass Transfer* **127**, 257–267.

JIANG, P.X., XU, Y.J., LV, J., SHI, R.F., HE, S. & JACKSON, J.D. 2004 Experimental investigation of convection heat transfer of CO_2 at super-critical pressures in vertical mini tubes and in porous media. *Appl. Therm. Engng* **24**, 1255–1270.

JIANG, P.X., ZHANG, Y., ZHAO, C.R. & SHI, R.F. 2008 Convection heat transfer of CO_2 at supercritical pressures in a vertical mini tube at relatively low Reynolds numbers. *Exp. Therm. Fluid Sci.* **32**, 1628–1637.

JIANG, P.X., ZHAO, C.R. & LIU, B. 2012 Flow and heat transfer characteristics of R22 and ethanol at supercritical pressures. *J. Supercrit. Fluids* **70**, 75–89.

JIANG, P.X., ZHAO, C.R., ZHANG, Y., SHI, R.F. & LI, Z.H. 2010 Convection heat transfer of CO2 at supercritical pressures in vertical small, mini and micro tubes. In *Proceedings of IAEA Technical Meeting on Heat Transfer, Thermal-Hydraulics and System Design for Supercritical Pressure Water Cooled Reactors*.

KIM, H., KIM, H.Y., SONG, J.H. & BAE, Y.Y. 2008 Heat transfer to supercritical pressure carbon dioxide flowing upward through tubes and a narrow annulus passage. *Prog. Nucl. Engng* **50**, 518–525.

KIM, J.K., JEON, H.K. & LEE, J.S. 2007 Wall temperature measurement and heat transfer correlation of turbulent supercritical carbon dioxide flow in vertical circular/non-circular tubes. *Nucl. Engng Des.* **237**, 1795–1802.

KIRILLOV, P.L., YUR'EV, Y.S. & BOBKOV, V.P. 1990 *Handbook of thermal–hydraulics calculation*. Energoatomizdat Publ. House.

KRASNOSHCHEKOV, E.A. & PROTOPOPOV, V.S. 1966 Experimental study of heat exchange incarbon dioxide in the supercritical range at high temperature drops. *Teplofiz. Vys. Temp.* **4**, 389–398.

LEE, J., JUNG, A.Y., SUNG, J.J. & ZAKI, T.A. 2013 Effect of wall heating on turbulent boundary layers with temperature-dependent viscosity. *J. Fluid Mech.* **726**, 196–225.

LEE, P.S., GARIMELLA, S.V. & LIU, D. 2005 Investigation of heat transfer in rectangular microchannels. *Intl J. Heat Mass Transfer* **48**, 1688–1704.

LEMMON, E.W., HUBER, M.L. & MCLINDEN, M.O. 2010 NIST standard reference database 23: reference fluid thermodynamic and transport properties-REFPROP, version 9.0. National Institute of Standards and Technology, Standard Reference Data Program.

LENG, C., WANG, X.D., YAN, W.M. & WANG, T.H. 2016 Heat transfer enhancement of microchannel heat sink using transcritical carbon dioxide as the coolant. *Energy Convers. Manage.* **110**, 154–164.

LIAO, S.M. & ZHAO, T.S. 2002 An experimental investigation of convection heat transfer to supercritical carbon dioxide in miniature tubes. *Intl J. Heat Mass Transfer* **25**, 5025–5034.

MAO, S., ZHOU, T., WEI, D., LIU, W.B. & ZHANG, T.T. 2021 Heat transfer characteristics of supercritical water in channels: a systematic literature review of 20 years of research. *Appl. Therm. Engng* **197**, 117403.

MAY, L. & BURKHARDT, W.M. 1991 Transpiration cooled throat for hydrocarbon rocket engines: contract NAS 8-36952. National Aeronautics and Space Administration.

MCELIGOT, D.M. & JACKSON, J.D. 2004 'Deterioration' criteria for convective heat transfer in gas flow through non-circular ducts. *Nucl. Engng Des.* **232**, 327–333.

MOHSENI, M. & BAZARGAN, M. 2011 The effect of the low Reynolds number $k-\varepsilon$ turbulence models on simulation of the enhanced and deteriorated convective heat transfer to the supercritical fluid flows. *Heat Mass Transfer* **47**, 609–619.

MUEGGENBURG, H.H., HIDAHL, J.W., KESSLER, E.L. & ROUSAR, D.C. 2010 Platelet actively cooled thermal management devices. In *Proceedings of AIAA 28th Joint Propulsion Conference and Exhibit*.

NARASIMHA, R. & SREENIVASAN, K.R. 1973 Relaminarization in highly accelerated turbulent boundary layers. *J. Fluid Mech.* **61**, 417–447.

NEMATI, H., PATEL, A., BOERSMA, B.J. & PECNIK, R. 2015 Mean statistics of a heated turbulent pipe flow at supercritical pressure. *Intl J. Heat Mass Transfer* **83**, 741–752.

NISHIKAWA, K., TANAKA, I. & AMEMIYA, Y. 1996 Small-angle X-ray scattering study of supercritical carbon dioxide. *J. Phys. Chem.* **100**, 418–421.

ORLANSKI, I. 1976 A simple boundary condition for unbounded hyperbolic flows. *J. Comput. Phys.* **21**, 251–269.

PATEL, A., PEETERS, J.W.R., BOERSMA, B.J. & PECNIK, R. 2015 Semi-local scaling and turbulence modulation in variable property turbulent channel flows. *Phys. Fluids* **27**, 095–101.

PEETERS, J., PECNIK, R., ROHDE, M., VAN DER HAGEN, T. & BOERSMA, B. 2016 Turbulence attenuation in simultaneously heated and cooled annular flows at supercritical pressure. *J. Fluid Mech.* **799**, 505–540.

PENG, X., PETERSON, G. & WANG, B. 1994 Frictional flow characteristics of water flowing through rectangular microchannels. *Expl Heat Transfer* **7**, 249–264.

PETUKHOV, B.S. 1977 Generalized correlations for local heat transfer coefficient for turbulent flow of water and carbon dioxide at supercritical pressure in uniformed heated tubes. *Teplofiz. Vys. Temp.* **15**, 815–821.

PETUKHOV, B.S, POLYAKOV, A.F. & LAUNDER, B.E. 1988 *Heat Transfer in Turbulent Mixed Convection*. Hemisphere.

PHILLIPS, R. 1990 Micro-channel heat sinks. In *Advances in Thermal Modeling of Electronic Components* (ed. A. Bar-Cohen & A.D. Kraus). ASME Press.

PIERCE, C.D. 2001 Progress-variable approach for large-eddy simulation of turbulent combustion school. PhD thesis, Stanford University.

PIERCE, C.D. & MOIN, P. 2004 Progress-variable approach for large-eddy simulation of non-premixed turbulent combustion. *J. Fluid Mech.* **504**, 73–97.

ROBEY, E.H., RAMESH, S., SABAU, A.S., ABDOLI, A., BLACK, J.B., STRAUB, D.L. & YIP, M.J. 2022 Design optimization of an additively manufactured prototype recuperator for supercritical CO2 power cycles. *Energy* **251**, 123961.

SCHOPPA, W. & HUSSAIN, F. 2002 Coherent structure generation in near-wall turbulence. *J. Fluid Mech.* **453**, 57–108.

SEDDIGHI, M. 2011 Study of turbulence and wall shear stress in unsteady flow over smooth and rough wall surfaces school. PhD thesis, University of Aberdeen.

WALL, C., PIERCE, C.D. & MOIN, P. 2002 A semi-implicit method for resolution of acoustic waves in low Mach number flows. *J. Comput. Phys.* **181**, 545–563.

YIN, L. & LIU, W.Q. 2018 Numerical investigation on the film cooling performance in a multi-elements splash platelet injector. *Acta Astronaut.* **152**, 458–467.

YOO, J.Y. 2013 The turbulent flows of supercritical fluids with heat transfer. *Annu. Rev. Fluid Mech.* **45**, 495–525.

YU, D., WARRINGTON, R., BARRON, R. & AMEEL, T. 1995 An experimental and theoretical investigation of fluid flow and heat transfer in microtubes. *Thermal engineering*, 523–530.

Zeighami, R.M., Laser, D., Zhou, P., Asheghi, M., Devasenathipathy, S., Kenny, T.W., Santiago, J.G. & Goodson, K.E. 2000 Experimental investigation of flow transition in microchannels using micron-resolution particle image velocimetry. In *Conference on Thermal and Thermomechanical Phenomena in Electronic Systems*. IEEE.

Zappoli, B., Beysens, D. & Garrabos, Y. 2014 *[Fluid Mechanics and its Applications] Heat Transfers and Related Effects in Supercritical Fluids*. Springer.

Zonta, F. 2013 Nusselt number and friction factor in thermally stratified turbulent channel flowunder non–Oberbeck–Boussinesq conditions. *Intl J. Heat Fluid Flow* **44**, 489–494.

Zonta, F., Marchioli, C. & Soldati, A. 2012*a* Modulation of turbulence in forced convection by temperature-dependent viscosity. *J. Fluid Mech.* **697**, 150–174.

Zonta, F., Marchioli, C. & Soldati, A. 2012*b* Turbulence and internal waves in stably–stratified channel flow with temperature–dependent fluid properties. *J. Fluid Mech.* **697**, 175–203.

Zonta, F. & Soldati, A. 2014 Effect of temperature dependent fluid properties on heat transfer in turbulent mixed convection. *Intl J. Heat Transfer* **136**, 022501.